Sedimentology, Biostratigraphy, Chemostratigraphy, and Sequence Stratigraphy of Middle Ordovician Strata, Inner Mongolia, China

A Senior Thesis Presented to

the Faculty of the Department of Geology

in Partial Fulfillment of the Bachelor of Arts Degree

Anne J. Hakim

Colorado College

May 2015

On my honor, I present this thesis to the faculty of the Geology Department of Colorado College as my own, in accordance with the Colorado College Honor Code.

Anne J. Hakim, May 2015

AKNOWLEDGEMENTS
Firstly, I would like to thank my advisor Paul Myrow for all of the incredible guidance, knowledge, and entertainment he shared over the last four years. Thank you also to Jitao Chen for his help navigating the world of Chinese geological literature, to Dr. Fike for the use of his mass spectrometer, to Dr. Leslie for his conodont analysis, to Zach Snyder for paving the way for this thesis with his, and to the Patricia K. Buster and Student-Faculty Collaborative grants for funding this project. Thank you to the entire Colorado College Geology Department for introducing me to the world of rocks, geodip, and stump. Shout out to the O. G. Geo Biddies, thank you for being my friends. Finally, thank you, Dad, Robert, and Noelle.

TABLE OF CONTENTS

FIGURES

PLATES

APPENDICES TO THE TEXT

ABSTRACT

Despite superb exposure of the Ordovician strata in the region, and detailed knowledge of the eastern and northeastern margins, the western margin of the North China Block (NCB) lacks an integrated study of sedimentology, biostratigraphy, and chemostratigraphy. This study presents such information, elucidating the depositional history and sequence stratigraphic framework of Middle Ordovician strata in Inner Mongolia, China. Two sections of the Middle Ordovician Kelimoli Formation contain the positive Middle-Darriwilian Carbon Isotope Excursion (MDICE), the first recorded evidence of MDICE in the region. Additionally, biostratigraphic data and previous research in the area allow for the proposal of a sequence stratigraphic framework for the NCB. Specifically, the disconformity at the base of the lowest Middle Ordovician Sandaokan Formation contains a sequence boundary between two megasequences, megasequences 1 and 2, in the lowermost Paleozoic (Myrow et al, *in press*; Meng et al., 1997). The Sandaokan, Zhuozhishan, and Kelimoli formations represent the first, second, and third sequences of megasequence 2, respectively. The Kelimoli Formation is overlain by a disconformity, which likely corresponds with the upper boundary of this megasequence and with globally widespread nondeposition according to biostratigraphic and chemostratigraphic correlation (Schmitz et al., 2010). This hypothesized sequence stratigraphic framework will be tested in the future with high-resolution biostratigraphic and chemostratigrpahic analysis of the Zhuozhishan Formation.

INTRODUCTION

The sedimentology and stratigraphy of Cambrian–Ordovician rocks of the western margin of the North China Block (NCB) are poorly understood, despite superb exposure of these units and a vast database of existing knowledge on the eastern and northeastern margins of the block (Meng et al., 1997; Chough et al., 2010; Lee and Chough, 2011). This study integrates sedimentological, biostratigraphic, and chemostratigraphic analyses of two sections of Middle Ordovician Kelimoli Formation in the western NCB with the goal of interpreting the paleoenvironments and depositional history, including relative changes in sea level, by using detailed measured stratigraphic sections, high-resolution carbon isotope curves, and conodont biostratigraphy. Chronostratigraphic ages of the sections are constrained using a combination of carbon isotope chemostratigraphic data and biostratigraphic data.

This work contributes to a larger project undertaken by Dr. Myrow and several collaborators that is aimed at producing a complete and detailed catalog of the western margin of the early Paleozoic NCB. This study will supplement the well-established database for the eastern margin, and will help create an integrated stratigraphy for the entire North China Platform (NCP). Correlation between the eastern and western margins is important because it allows for the recognition of changes in depositional systems across the NCP for several time slices in the early Paleozoic. The sedimentological and stratigraphic signal, including sequence-stratigraphic architecture, as well as biofacies and lithofacies patterns, may allow for the identification of a conjugate passive margin of the NCB that developed during Neoproterozoic rifting. More specifically, paleogeographic reconstructions of the Neoproterozoic through Paleozoic for this region

suggest that a landmass broke off from the western margin of the NCB, although its identity is uncertain (Myrow et al., *in press*). It is hoped that comparison of details of sedimentological and stratigraphic signatures of Paleozoic strata, and associated unconformites, may help with future reconstructions (Myrow et al., *in press*).

GEOLOGIC BACKGROUND

Modern China is comprised of three major continental-scale cratonic masses: the Tarim, South China/Yangtze, and North China blocks (NCB) (Huang et al., 2000). The NCB covers an area of 1,500 km east–west and 1,000 km north–south, and its limits are defined by tectonic boundaries (Fig. 1) (Meng et al., 1997). The northern edge of the NCB is delineated by the Junggar–Hingan fault and suture zone, which formed during the Permian collision of the NCB with the Mongolian plate (Meng et al., 1997; Lee and Chough, 2010). The southern and southwestern borders of the block are marked by the middle of the Kunlun–Qilian–Qinling Tectonic Belt, a set of Late Ordovician to Early Silurian structures that formed during accretion of microtectonic blocks onto the southern margin of the NCB (Meng et al., 1997; Bian et al., 2001). The eastern margin of the block is defined by the major sinistral strike-slip Tanlu Fault, which formed as a result of collision with South China (Meng et al., 1997; Lee and Chough, 2011). The northwest margin of the block is difficult to define, but is characterized by a thick succession of strata deposited in the northeast-trending Helan Aulacogen, a failed third arm of a triple junction, which formed in the Mesoproterozoic (Sun and Liu, 1983; Lin et al., 1991; Darby and Ritts, 2002).

In the NCB, Archean metamorphic rocks are nonconformably overlain by Cambrian strata, which are disconformably overlain by Middle Ordovician strata. The NCB was inundated during the early Cambrian global transgression, allowing for the development of a vast epeiric platform onto which a thick (up to 1,800 m) succession of mixed carbonate and siliciclastic deposits accumulated (Meng et al., 1997; Chough et al., 2010). The relatively flat surface of the craton remained submerged, except for some scattered

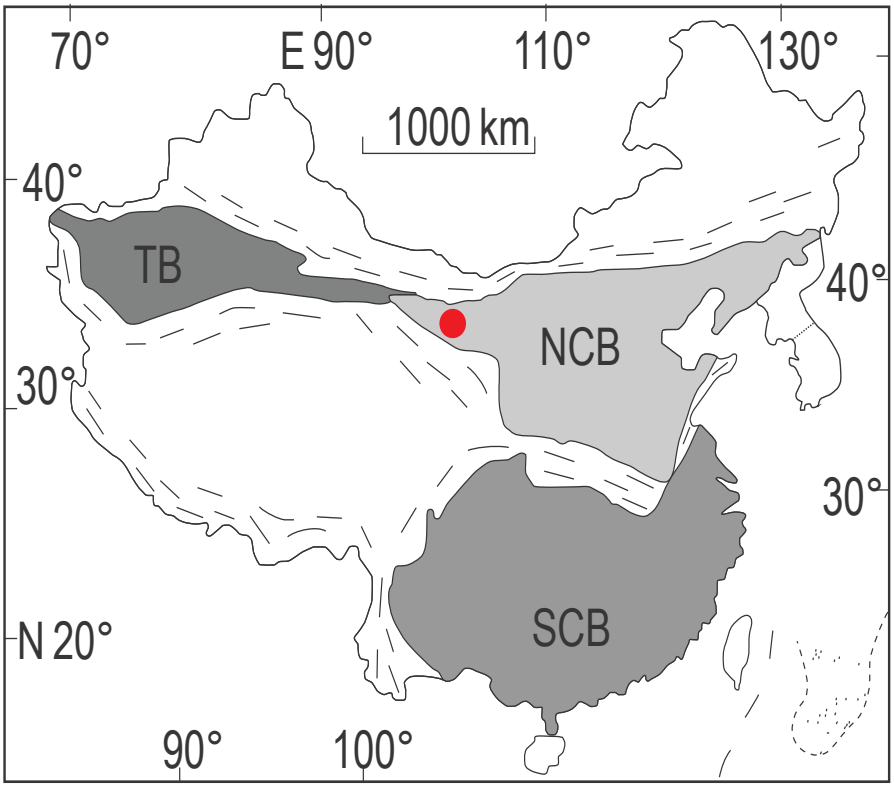

Figure 1. Simplified lithotectonic map of mainland China showing lithotectonic blocks. The red dot marks the study area. TB = Tarim Block, NCB = North China Block, SCB = South China Block (adapted from Myrow et al., *in press).*

archipelagos in the northwest, as transgression initiated from the southeast (Meng et al., 1997; Lee and Chough, 2011). These archipelagos served as highlands that shed fine siliciclastic sediment into the ocean, where it was distributed by tidal currents (Lee and Chough, 2011). Throughout the Ordovician, the NCB was dominated by a marine depositional environment. The Ordovician units in the western NCB are the Zhuozhishan, Kelimoli, Wulalike, Lashenzhong, Gongwusu, and Sheshan formations from oldest to youngest, respectively (Fig. 2).

The sedimentology, paleontology, stratigraphy, and tectonic evolution of the eastern margin of the NCB have been extensively studied (e.g., Chough et al., 2010; Lee and Chough, 2011), but little is known about the western margin. Conodont biozones have been determined for one outcrop of Kelimoli Formation in the western NCB (Wang et al., 2013). However, that study lacks detailed sedimentological descriptions. Sedimentological interpretations are of interest for the western NCB, in part because the sedimentological patterns and lithofacies there were influenced by both the presence of the highlands (absent in the eastern NCB) and deposition within the Helan Aulacogen (Myrow et al., *in review*). In this study I integrate biostratigraphic and sedimentologic data for the Kelimoli Formation in order to place it in regional paleoenvironmental and chronostratigraphic context and to propose a sequence stratigraphic framework for the NCB.

Chronostratigraphy		Formation	Major Lithology
Upper Ordovician	Bashkirian	Yanghugou	Sandstone, coal, shale, limestone
	Katian	Sheshan	Turbidite sandstone, siltstone, shale, bioclastic grainstone
	Sandbian	Gongwusu	Greenish-gray mudstone, thin-bedded limestone, sandstone
		Lashenzhong	Turbidite sandstone, siltstone, shale
		Wulalike	Slump-debris flow deposits, black shale
Middle Ordovician	Darriwilian	Kelimoli	Graptolitic black shale, thin-bedded limestone, turbidite
		Zhuozhishan	Bioturbated and bioclastic limestone, microbialites
		Sandaokan	Quartzose sandstone, bioclastic dolostone, limestone

Figure 2. Middle through Upper Ordovician stratigrahpy of the western Inner Mongolia and Ningxia regions of the North China Block (adapted from Myrow et al., *in press*).

STUDY LOCATIONS AND PREVIOUS WORK

In this study I describe and analyze results from two stratigraphic sections of Ordovician rocks in Inner Mongolia, China. The first locality, Yixiantian (YXT), lies approximately 20 km south of Wuhai (Fig. 3). Wang et al. (2013) previously studied this locality, and refer to it as the Dashimen locality. The second locality, Xilaifeng (XLF), is located approximately 30 km south of Wuhai (Fig. 3) on Zhuozhishan Mountain, a large basement-cored anticline (Darby and Ritts, 2002).

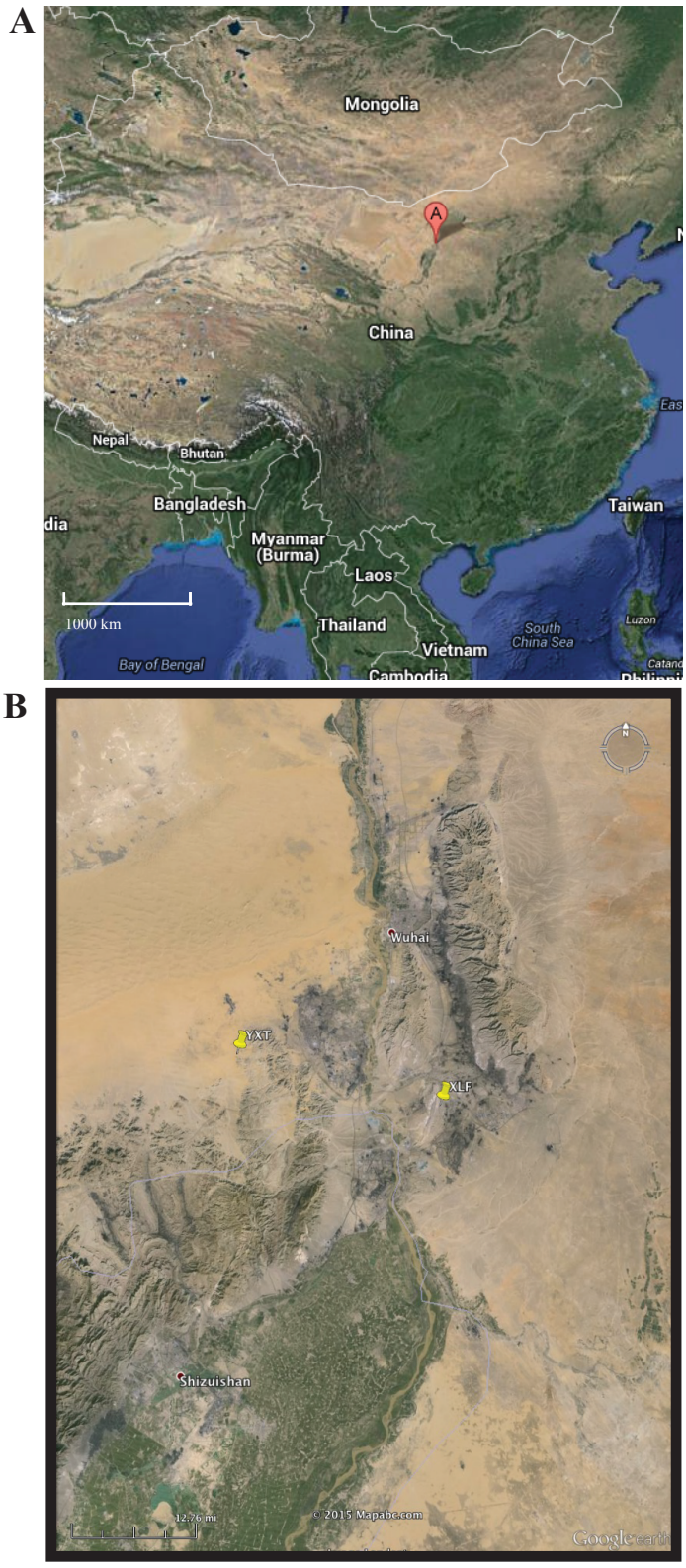

Figure 3. Study site locations (A) map from Google Earth, marking general location of study sites with a red bubble labeled A (B) Detailed view of red bubble A showing YXT and XLF localities relative to Wuhai.

METHODS

Field Methods

Fieldwork for this study was completed, in part, in July 2013 with Dr. Paul Myrow and Dr. Jitao Chen. We measured XLF (185 m thick) and described it in detail, collected samples of carbonate-bearing rocks every 0.5 m for isotopic analysis, and every 10 m for conodont analysis over the entirety of the section. Additionally, we measured the orientations of 100 imbricated clasts at a breccia bed at 174.97 m. The clasts were randomly selected, measured at least 10 cm along their longest axis, and were exposed in three dimensions in order to obtain reliable geometric measurements. These data were imported into the computer program Stereonet, rotated to paleohorizontal, and plotted on a lower-hemisphere rose diagram. In July 2014, Drs. Myrow and Chen returned to Inner Mongolia to repeat the sedimentology, chemostratigrpahy, and conodont sampling at YXT (67 m thick).

Chemostratigraphy

This part of the study combines the techniques of stable isotope geochemistry and stratigraphy in order to create a record of isotopic change, which can be used to precisely correlate these sections with others and to and refine their ages. Stable isotope geochemistry uses the ratio of different isotopes of a single element to measure fractionation, the separation of isotopes by chemical, physical, or biological processes. The difference in mass between isotopes causes them to form bonds of differing strengths with other atoms. This ultimately causes the isotopes to behave differently in chemical reactions which may prefer one isotope over the other (Ripperdan, 2001). Thus, products

can have very different ratios of stable isotopes than reactants, and isotopic ratio of the product can serve as a signature for a particular chemical reaction. This makes it possible to use stable isotope ratios to trace the movement of elements as they cycle within and between geochemical reservoirs (Ripperdan, 2001).

This study uses carbon isotope chemostratigraphy, in which the ratio of ^{13}C to ^{12}C in carbonate minerals from stratigraphically ordered samples are used to create a chemostratigraphic curve that acts as a section's geochemical fingerprint. I present such curves for the XLF and YXT. This ratio is represented by $\delta^{13}C$ (Equation 1).

(Eq. 1) $$\delta_{sample} = [(R_{sample}/R_{standard}) - 1] \times 10^3$$

In this equation, δ_{sample} is $\delta^{13}C$ measured in per mil (‰), R_{sample} is the ratio $^{13}C/^{12}C$ of in a sample, while $R_{standard}$ is $^{13}C/^{12}C$ for a known standard. This equation gives values that represent the deviation in $^{13}C/^{12}C$ of a sample from the standard value. This study uses the Vienna Pee Dee Belemnite standard. More specifically, positive $\delta^{13}C$ values indicate that the sample is enriched in ^{13}C relative to the standard, while negative $\delta^{13}C$ values indicate ^{13}C depletion.

The Carbon Cycle

Carbonate minerals crystallize from ocean surface water, and are in equilibrium with ambient water at the time of crystallization with regard to $\delta^{13}C$. Therefore, marine carbonate $\delta^{13}C$ values reflect the $\delta^{13}C$ of the surface water of the ocean. The $\delta^{13}C$ of

shallow ocean water is controlled by the global carbon cycle, which has long-term and short-term components that trace the path of carbon through four major reservoirs: the lithosphere, hydrosphere, atmosphere, and biosphere (Fig. 4). The long-term carbon cycle refers to the transfer of carbon from deep crustal and mantle reservoirs to the shallow crustal reservoir by the ocean–atmosphere system, which passes carbon through several reactive pathways, changing $\delta^{13}C$ values as carbon leaves and reenters the lithospheric reservoir. (Ripperdan, 2001)

The short-term cycle is comprised of the movement of carbon between and through the atmosphere, hydrosphere, and biosphere along many reaction pathways. The relatively high reaction rates in the short-term cycle, paired with the large isotopic fractionations that occur along the way, allow for geologically rapid isotopic modification of the marine carbon reservoir. The most influential process that occurs during the short-term cycle is photosynthesis, which entrains carbon from both atmospheric and marine reservoirs in biological compounds with a strong preference for ^{12}C. $\delta^{13}C$ values of the atmosphere and hydrosphere decrease as a result of photosynthetic carbon fractionation.

The long-term cycle is comprised of interaction of the lithosphere with the short-term cycle. The addition of lithospheric carbon in the form of bicarbonate, carbon dioxide, and methane to the ocean–atmosphere system by volcanic, metamorphic, and diagenetic degassing and weathering is balanced by the removal of sedimentary carbon compounds from the surface ocean. This system is kept close to steady state on a geologic scale by an array of feedback mechanisms.

At the global scale, carbon isotope ratios of the surface ocean are relatively homogenous at any given time as a result of ocean circulation. More specifically, carbon

isotope equilibrium exists between the atmosphere and the surface ocean, which is maintained through gas exchange and turbulent mixing, and acts on a relatively short time scale. Any isotopic irregularities that occur in the surface ocean as the result of atmosphere-ocean exchange processes are rapidly and evenly distributed by ocean circulation. In this way, the surface ocean serves as a globally homogenous carbon reservoir on a long-term global scale, which allows for the use of stratigraphic $\delta^{13}C$ curves as global signals.

While the $\delta^{13}C$ of the marine reservoir is homogenous at a given time, the $\delta^{13}C$ of the surface ocean changes over time in response to many factors that include, but are not limited to, changes in the following: biological productivity level, continental weathering during continental uplift, sea surface temperature, oceanic circulation, outgassing, and removal of carbon by sedimentary burial. The number and complexity of the processes that control the isotopic carbon ratio of the surface ocean make $\delta^{13}C$ values generally non-diagnostic as paleoenvironmental indicators when they are not paired with other geochemical data because of the complex interrelationships of these processes. Therefore, the actual $\delta^{13}C$ values themselves are not useful in this study, but the overall shape of the $\delta^{13}C$ curve is useful for global correlation.

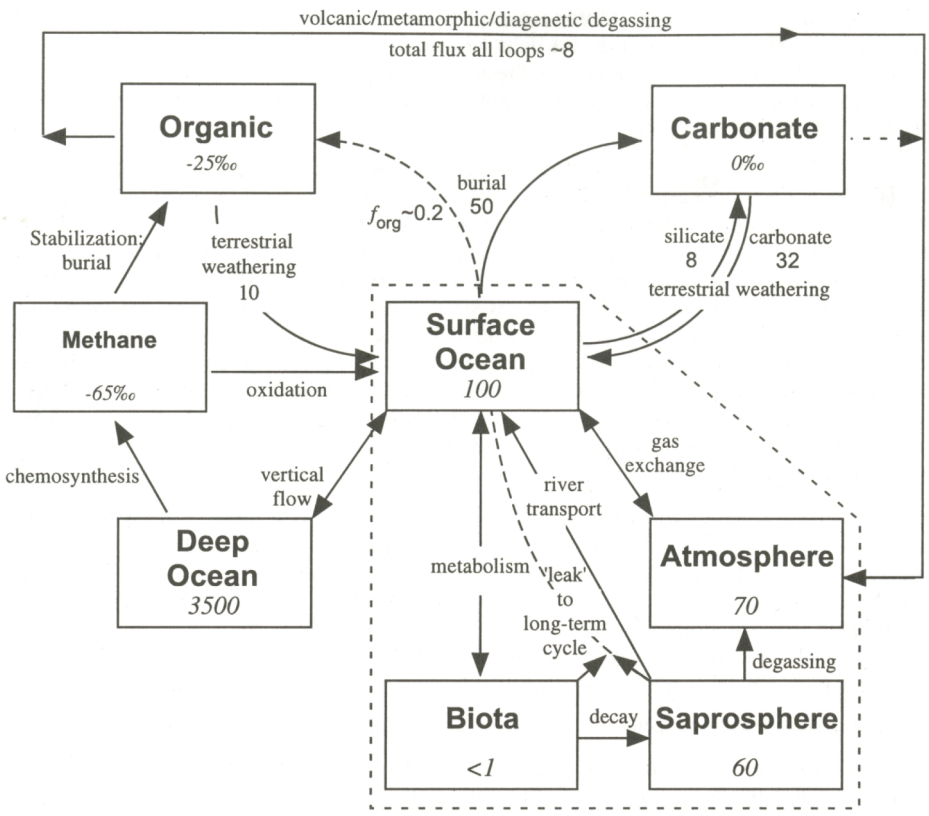

Figure 4. A schematic diagram of the carbon cycle from Ripperdan (2001) showing reservior sizes (Gmoles), flux estimates (Gmoles/ky), and isotopic values (permil VPDB) relative to the Phanerozoic. The section enclosed by the dotted line represents the short-term carbon cycle, while all processes outside of the dotted line belong to the

Field and Laboratory Techniques

A carbonate sample was taken approximately every 0.5 m for the entirety of the XLF and YXT sections where carbonate is present. Samples were cut and microdrilled with a dental drill bit for powder at Colorado College before being analyzed at the Stable Isotope Biogeochemistry Laboratory at Washington University in St Louis, Missouri. Each individual aliquot of approximately 150 μg of carbonate powder was reacted with excess of 100% H_3PO_4 in He-flushed sealed tubes for 4 hours at 72°C in order to prevent the contamination of the sample carbon dioxide with modern atmospheric carbon dioxide. Evolved carbon dioxide samples were then sampled using a Finnigan Gas Bench II, and isotopic ratios were measured using a Delta V Plus Mass Spectrometer, which uses an electromagnetic field to separate molecules by mass. Isotopic measurements were calibrated against the standards NBS-19 and NBS-20, as well as two in-house standards. The measurements obtained were then calibrated to the Vienna Peedee Belemnite (VPDB) standard. The data were then graphed stratigraphically, and the resultant curves were compared to each other and known global $\delta^{13}C$ curves for the same time period.

SEDIMENTOLOGY

Results

Outcrop Descriptions

YXT

The section is approximately 67 m thick (Appendix A). Its base is defined by the contact between massive limestone of the Zhuozhishan Formation and interbedded mudstone and marl facies of the Kelimoli Formation. The total thickness of the basal mudstone and marl facies is approximately 43 m (lower Kelimoli Formation) This facies is overlain by ~17 m of graptolitic black shale (upper Kelimoli Formation), the top of which is an irregular contact between the shale and overlying breccia, the latter of which represents the base of the Wulalike Formation (Wang et al., 2013).

XLF

XLF is comprised of 185 m of mixed carbonate and siliciclastic rocks, predominantly finely laminated interbedded carbonate mudstone and marl with relatively abundant soft sediment deformation structures (Appendix B). This facies makes up the lower 170 m of the section (lower Kelimoli Formation), contains abundant trilobites, and is overlain by grainstone, graptolitic black shale (upper Kelimoli Formation), and breccia facies, respectively. The breccia is comprised of angular imbricated intraclasts of tabular white mudstone and gray siltstone with medium gray, very coarse petroliferous grainstone matrix. The breccia defines the base of the Wulalike Formation (Wang et al., 2013). The contact between the Kelimoli Formation and the underlying Zhuozhishan Formation (massive limestone) is either below the base of the section, or there is a major facies

change so that the lower Kelimoli includes age-equivalent rocks to the thick massive carbonate of the Zhuozhishan.

Facies Descriptions

Interbedded Mudstone and Marl

This facies is composed of intercalated tabular mudstone beds and 10% to 15% recessive marl beds (Plate 1). The mudstone is dark gray and weathers white. It is comprised of a mixture of alternating, fine, 1 to 6 mm thick, parallel, white micritic laminae, and a lesser percentage of 1 to 2 mm thick calcisilitite laminae. The mudstone beds range from 2 to 15 cm thick, with an average thickness of 10 cm, whereas the marl beds are generally less than 1 cm thick. The mudstone contains relatively abundant trilobites fragments and specimens that generally have a nearly complete thorax and pygidium.

Siltite

Siltite is a slightly coarser facies than mudstone, made up solely of carbonate silt-sized particles. It is gradational with the mudstone, and lacks the lamination present in the mudstone facies and siliciclastic input. It is light gray and beds are 3 to 7 cm thick.

Plate 1:
Interbedded Mudstone and Marl

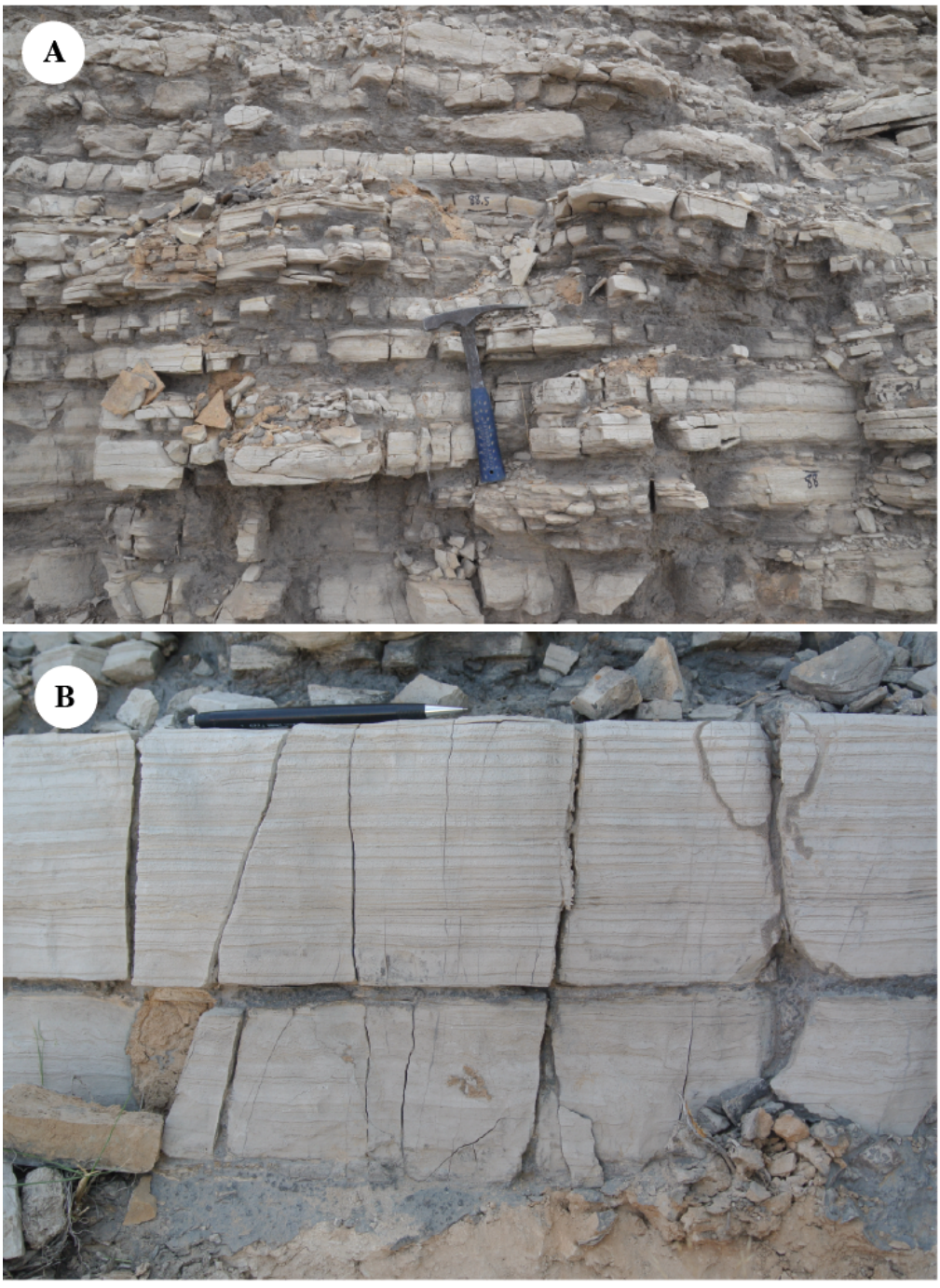

Plate 1. (A) Interbedded mudstone and marl (B) finely laminated mudstone

Disturbed Beds

The disturbed beds are lithologically composed of the same material as the interbedded mudstone and marl facies, and are defined by slumped bedding to intricately convoluted laminae (Plate 2). Beds range from 21 cm to 79 cm thick, averaging approximately 50 cm. In cases, the bedding is deformed into nearly recumbent folds with clearly exposed fold hinges. The direction of closure of 12 fold hinges was inferred from their measured orientations (Fig. 5), and they close uniformly towards the east–southeast, with a vector mean of 119.6°. The disturbed beds are laterally discontinuous, pinching out into horizontally bedded strata in some places, and are in abrupt contact with undeformed horizontal beds in others. There is also some local brecciation (e.g., 99 to 100 m at XLF), where there are flat-pebble lenses within the soft-sediment folds.

Graptolitic Black Shale

This facies is characterized by dark gray to black, fissile, silty shale with abundant sand-sized pyrite crystals and abundant graptolite fossils. The facies exists at comprises the top ~17 m of YXT, and one 4.8 m thick stratigraphic interval at 170.67 m at XLF.

Grainstone

This facies varies from medium to very coarse grainstone with skeletal fragments (Plate 3). Beds are generally coarser and more abundant upsection, and range from 10 cm to 70 cm thick. In places, 2 cm to 13 cm of discontinuous white weathering mudstone separates grainstone beds. Approximately 40% of the grainstone beds exhibit 10 cm to 37 cm thick

Plate 2:
Disturbed Beds

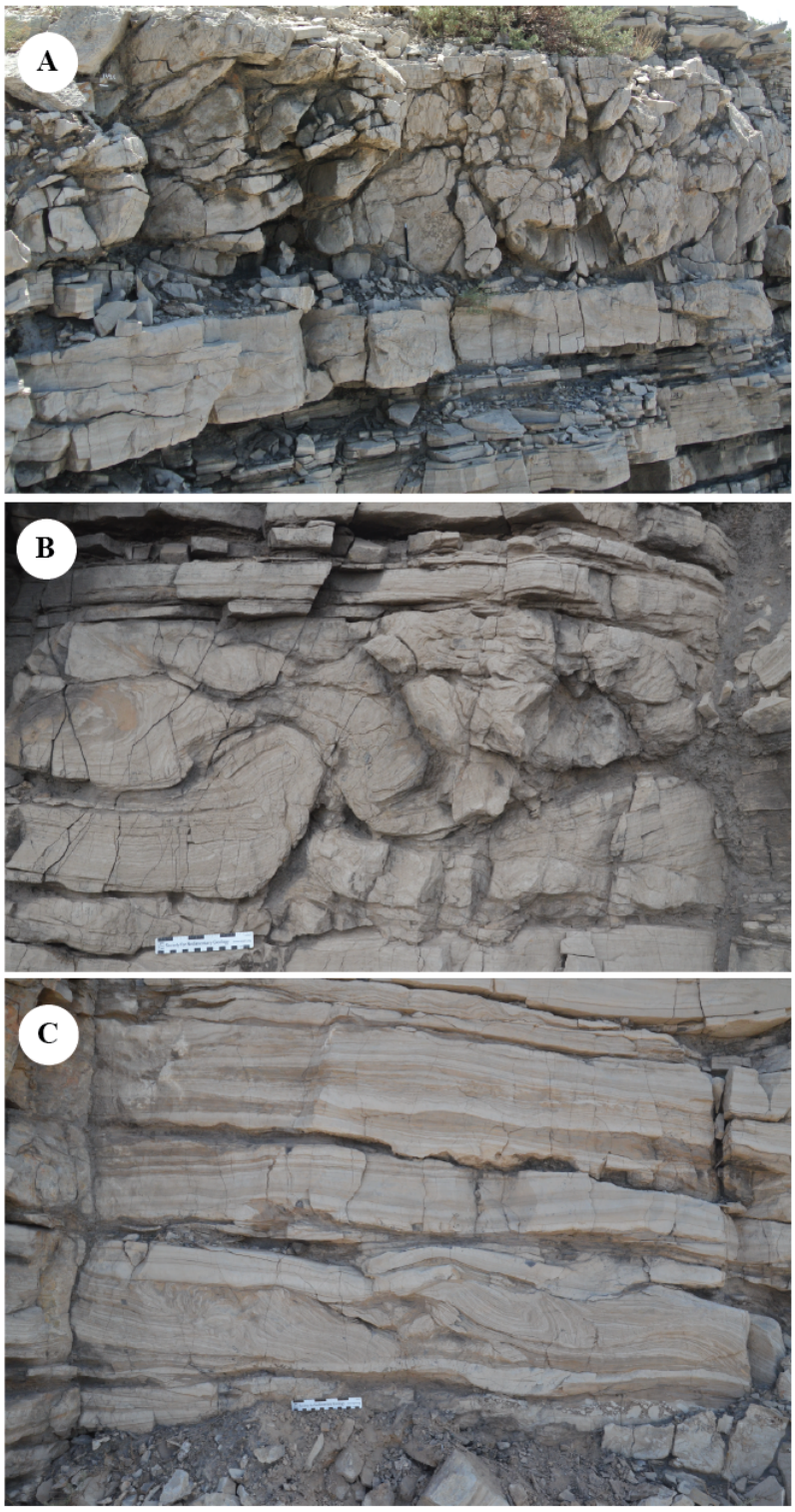

Plate 2. (A) Clinoformed slumped bedding (B) Deformed beds with deformed lamination (C) Intricately convoluted laminae

cross-bed sets. The grainstone locally makes up gutter casts, and generally forms lenses encased within carbonate mudstone. Some grainstone beds contain tabular intraclasts of mudstone.

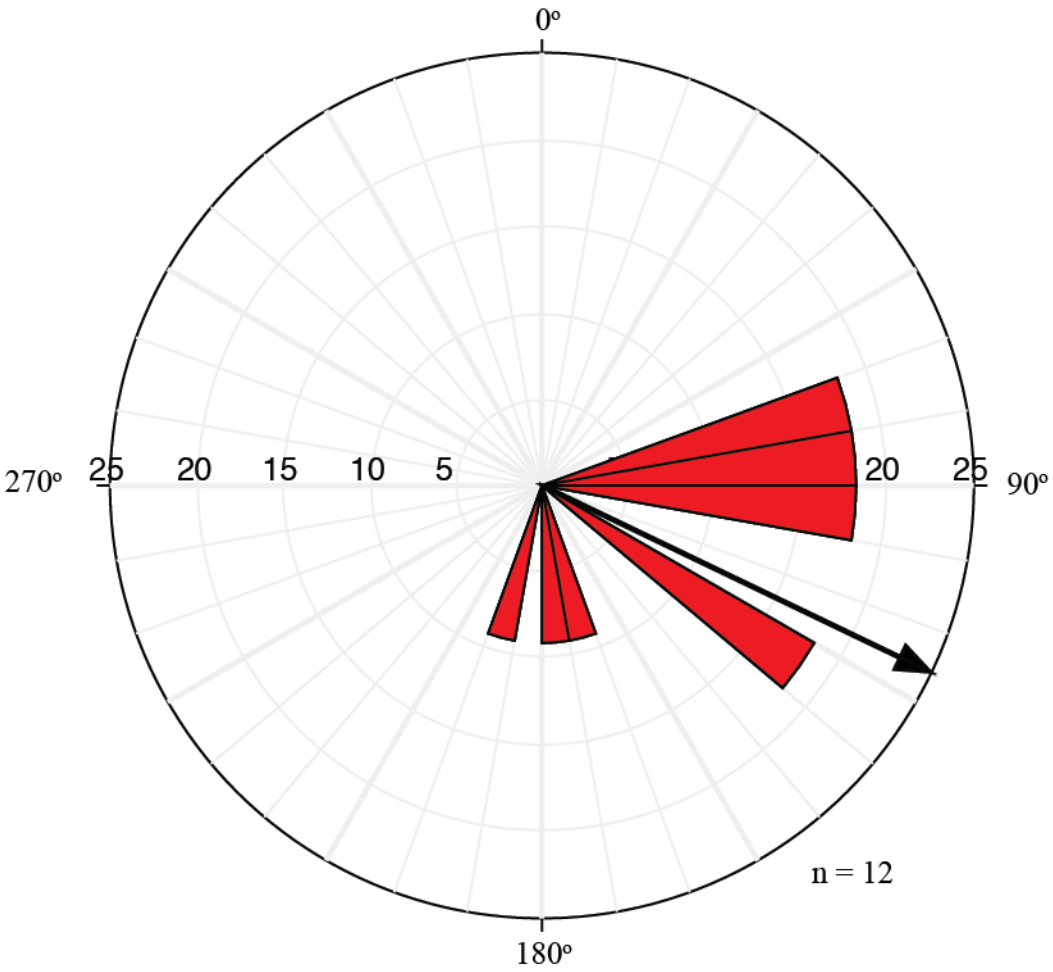

Figure 5. Rose diagram of inferred downhill direction from geometric orientation data from 12 folds in the disturbed beds facies. The horizontal axis represents percentage of beds that fall into each 10° bin. The black arrow is the mean vector, and shows that the dominant downhill direction was 119.6°. Additionally, 36.36% between 91° and 100°.

Plate 3:
Graptolitic Black Shale and Grainstone

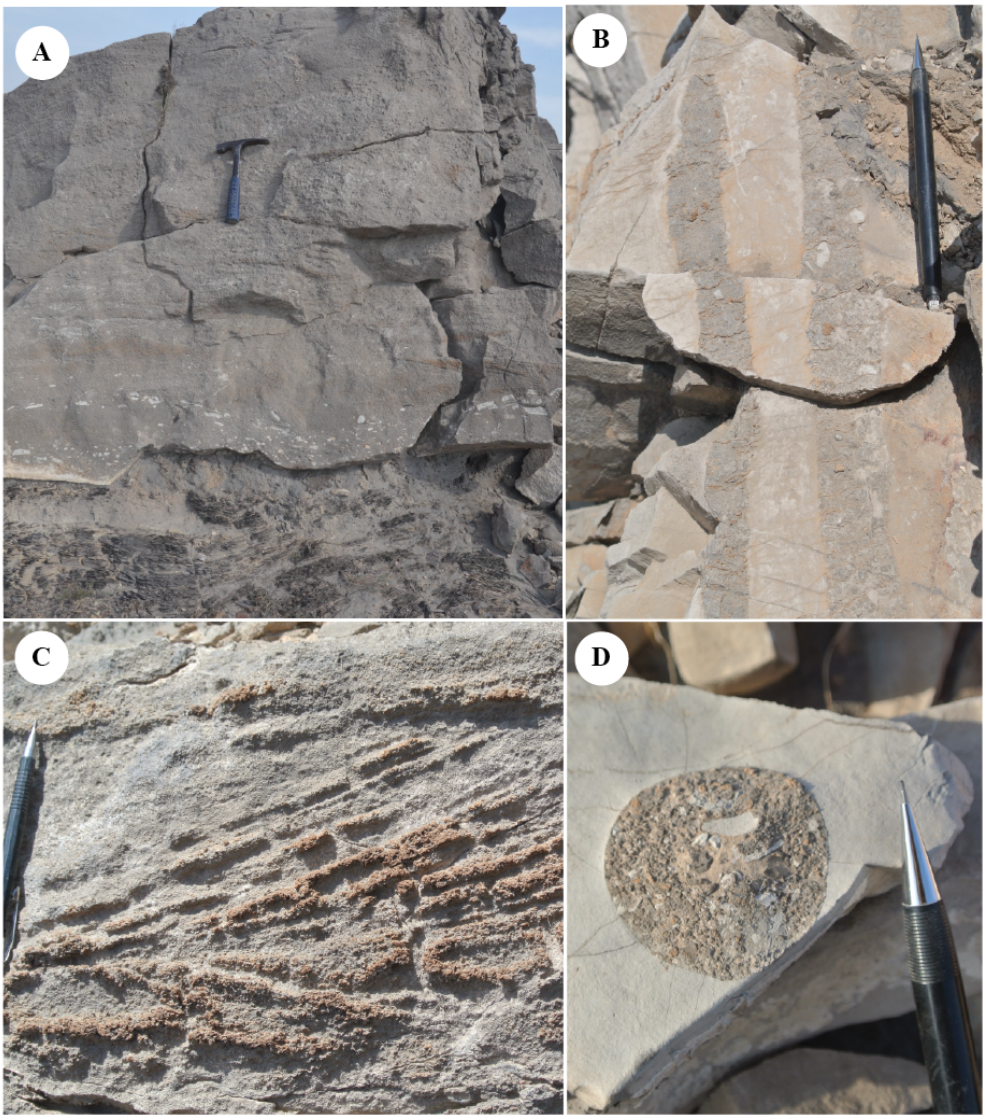

Plate 3. (A) Contact between the graptolitic black shale (below) and grainstone (above) facies (B) Mudstone ripples filled with grainstone (C) Crossbedding in grainstone (D) Mustone pot cast with grainstone fill

Breccia

Very coarse breccia makes up two beds near the top of the section at XLF: a 2.1 m thick bed at 174.97 m, and a 4.46 m thick bed at 182.64 m (Plate 4). In the lower 2.1 m thick bed, the breccia is composed of imbricated, tabular, angular, white mudstone and gray siltstone intraclasts of similar composition to the underlying mudstone succession, along with medium gray very coarse petroliferous grainstone matrix. The planar orientations of 100 clasts of at least 10 cm in length were measured in this bed in order to obtain a paleocurrent flow direction. The rose diagram (Fig. 6) shows that the measured intraclasts record paleoflow directions that uniformly point between the west and southeast, with a vector mean of 274.9°.

The lower 2.1 m thick bed varies texturally with stratigraphic height, and has three distinct divisions. The lowest textural division of the bed (174.97 m to 176.63 m) is clast supported and has the largest intraclasts in the beds of this facies, which measure up to 70 cm by 9 cm in cross-section. The second division consists of a layer of smaller matrix-supported clasts (176.63 m to 176.73 m). The third division of the first breccia bed, which is barely matrix-supported, contains intermediate-sized angular intraclasts that reach 60 cm by 6 cm, and average 30 cm by 5 cm.

The stratigraphically higher 4.46 m thick bed is a clast-supported breccia that also varies texturally with stratigraphic height. A lowest division is 36 cm thick (182.64 m to 183 m) and contains a combination of 75% white mudstone intraclasts and 25% grainstone intraclasts, which are contained in a coarse mudstone matrix. From 183 m to 184.51 m, the intraclasts are larger, with the largest mudstone intraclast measuring 23 cm x 20 cm x 5 cm, and the largest grainstone intraclast measuring 46 cm x 5 cm x 24 cm.

From 184.51 to 185 m, the breccia contains 80% mudstone clasts and 20% grainstone intraclasts in a matrix of coarse grainstone. Here, the grainstone intraclasts are much smaller, with the largest measuring 7 cm x 5 cm in cross-section.

Plate 4:
Breccia

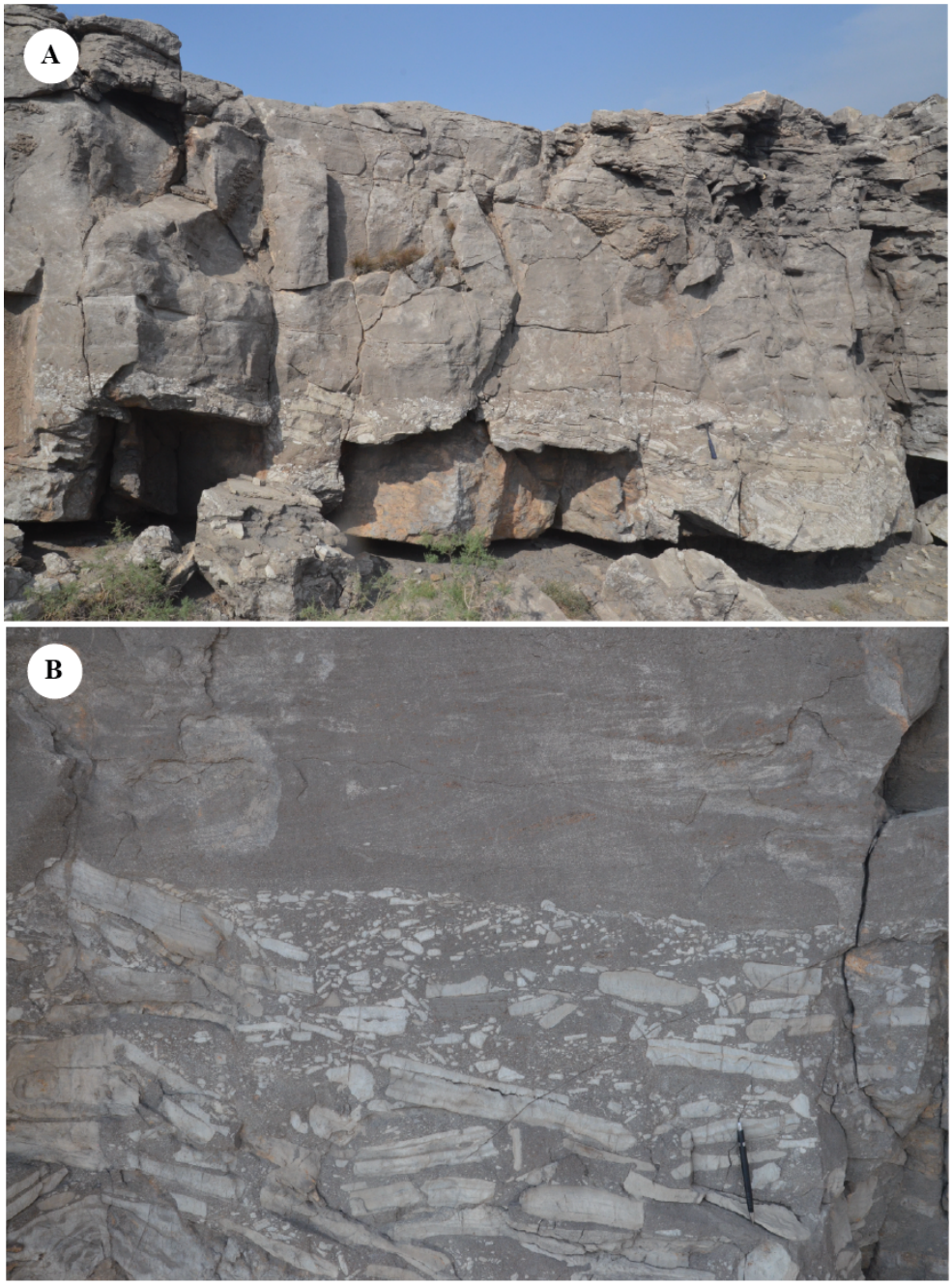

Plate 4. (A) Contact between breccia (below) and grainstone facies (above). (B) Close-up of the contact from image A. Notice the mudstone intraclasts and crossbeds within the grainstone.

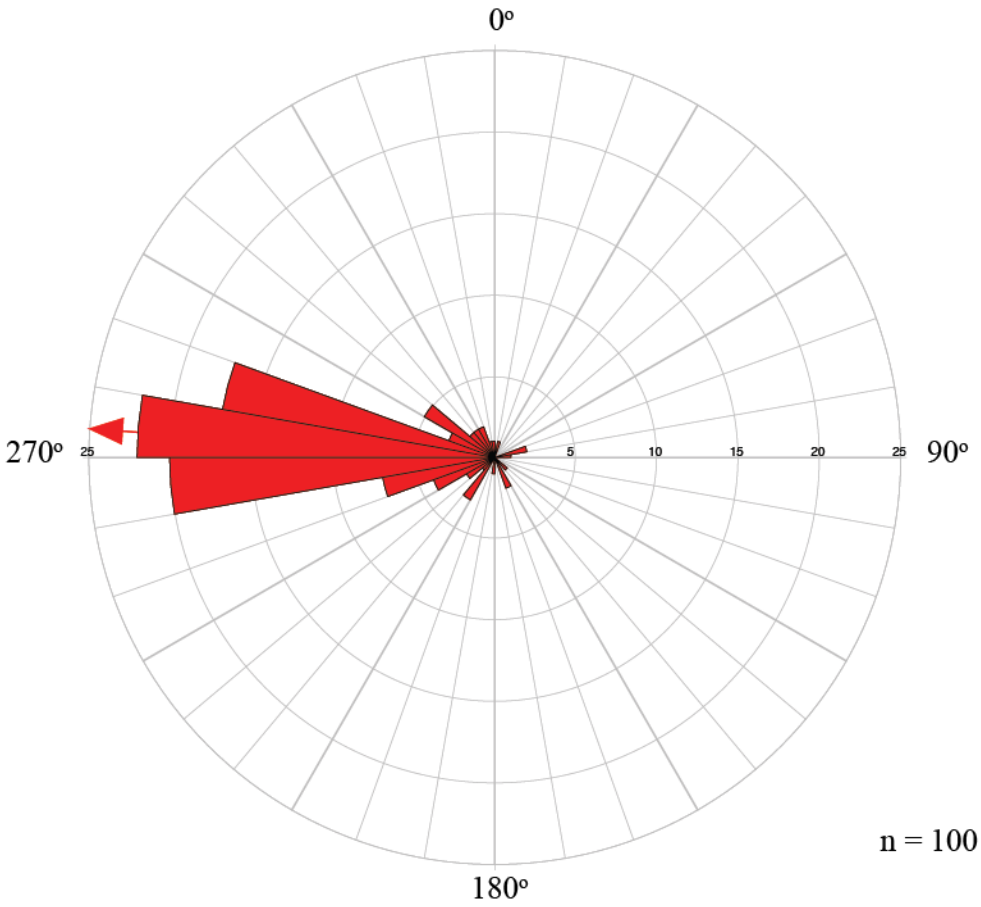

Figure 6. Rose diagram showing inferred paleocurrent direction from clasts measured in bed at 174.97 m. Bins are set to 10° and, the scale on the horizontal axis shows percentage up to 25%. The red arrow is the mean vector, and shows that the dominant flow direction was 274.9°. Additionally, 22% of the data fell between 271° and 280°.

Facies Interpretations

Interbedded Carbonate Mudstone and Marl

Interbedded laminated carbonate mudstone and marl suggests alternating deposition of carbonate and mixed carbonate and siliciclastic material in a marine environment. Clay-size particles in both the marl and mudstone indicate that sedimentation occurred by suspension in a low-energy setting. The lamination in the mudstone reflects slight changes in grain size that might be linked to weak changes in currents. The marl reflects periods of input of terrestrial mud that was being mixed with carbonate mud in the water column. The total lack of traction-generated features, and sandy facies in general, over such a stratigraphic thickness suggests uniform low energy conditions consistent with deeper marine deposition.

The time scale associated with deposition of each of these lithologies is not known, so it is not clear whether the mudstone or marl beds represent individual events, or longer-term changes in input of either carbonate or siliciclastic mud. Long-term changes in terrigenous mud input could be linked to changes in base level or terrestrial runoff by a process such as changes in climate.

Siltite

The siltite and carbonate mudstone and marl facies were deposited in the same environment with variations in current strength. The grain size is slightly greater than the mudstone, but still so small that deposition also took place from suspension, but under slightly higher energy conditions. ,The silitite is gradational with the mudstone, suggesting that current strength gradually transitioned.

Disturbed Beds

Based on the fact that the deformed beds are lithologically identical to the mudstone and marl facies, the folding and convolution patterns of the deformed beds are consistent with soft-sediment deformation patterns produced in slump deposits in marine slope environments (Drzewiecki and Simo, 2002; Tucker and Wright, 1990). More specifically, the mass movement of soft sediment down slopes commonly results in the internal rotation of sediment masses within a transported lobe along a defined shear plane, resulting in a range of fabrics from simple folds to convolutions (Drzewieci and Simo, 2002; Tucker and Wright, 1990; Mullins and Cook, 1986; Stow, 1986; Lowe, 1982). It is likely that the sliding material contained some well-lithified mudstone, given the evidence for local brecciation, but this is the exception, not the norm. The geometric analysis of the 12 folds indicates that the dominant direction of fold closure, and thus the dominant downhill direction, was east–southeast. This is a weak inference because only a few folds were exposed in three-dimensions for accurate measurement. However, the fact that the downhill direction for all of the folds generally points in the same direction with no outliers suggests that the mean vector gives a rough approximation to the paleodownhill direction.

Graptolitic Black Shale

The shale facies represents dominant siliciclastic sediment input and low levels of carbonate production, possibly linked to an increase in water depth (Tucker and Wright, 1990). The dark color of the shale reflects high organic content and the presence of disseminated pyrite, and is indicative of relatively reducing conditions (Myrow, 1990).

Grainstone

The medium to coarse grainstone was deposited by the reworking of carbonate and skeletal sand at lower water depth and in a higher energy environment than the mudstone and marl facies (Pomar et al., 2004; Tucker and Wright, 1990). The cross-bedding indicates deposition under the influence of unidirectional currents that produced migrating small dunes (Pomar et al., 2004).

Breccia

The breccia facies is consistent with deposition by mass transport within a channel on a submarine fan (Spatelli et al., 1998). The breccia shows both clast-supported and grainstone-supported intervals, suggesting multiple mass transport events or changes in the rheology and physical states of the flows over time.

The alternating textural patterns within the lower 2.1 m debris flow deposit are particularly distinct and suggest that at times the flow was concentrated but driven by the fluid,and at other times the flow was likely more viscous and/or hyperconcentrated (Stow and Mayall, 2000). Upward changes from clast-supported, to matrix-supported, to barley matrix-supported reflect significant variability in sediment concentration and flow behavior. Some beds show changes in the average size of clasts between divisions, which speaks to the overall intensities of the flows. These textural variations suggest that either the flow mechanism changed during the deposition of individual beds, or that there were multiple mass transport flow events recorded.

Specifically, it is possible that the lower 1.76 m (which includes the first and second textural divisions) of the breccia unit was deposited by a single decelerating fluid-rich

flow. This interpretation is based on the clast-supported nature of this unit; in a fluid-rich flow, the clasts and the matrix are transported individually within a moving dispersion, depositing the unit from the bottom up, and thus exhibiting normal grading (Tucker and Wright, 1990). After deposition of the lower two divisions, this flow either ceased, in which case the upper division was deposited by a much later flow, or a matrix-supported debris flow containing intermediate size clasts was emplaced on top of it shortly thereafter, as part of the same failure event (Tucker and Wright, 1990).

Geometric analysis of imbricated clasts measured at bed 174.97 m indicates that the inferred direction of paleoflow (Spaletti et al., 1989) was to the west (vector mean of 274.9°). The data are unimodal and do not show any outliers, indicating that either this flow was likely channelized and constricted by the channel walls.

The upper 4.46 m thick debris flow unit also contains textural variation. The overall composition of the clasts becomes slightly more mudstone-dominated upsection, and the composition of the matrix transitions from mustone to grainstone. However, the unit remains matrix-supported throughout, suggesting that the debris flows were dominant for the deposition of this unit, but that the source material changed (Tucker and Wright, 1990).

Depositional Model

The lithofacies present at XLF and YXT indicate deposition on a submarine apron, which is consistent with a previous depositional model proposed for the Kelimoli Formation in Inner Mongolia by Lin et al. (1991), who interpreted both submarine fan and carbonate apron depositional mechanisms within the Kelimoli Formation. The submarine fan

deposits contain lenticular channel-fill and sheet-like calcareous breccias of debris flow deposits on the inner fan, lenticular massive sandstone and conglomerate that formed in braided channels, and interbedded shale and turbidite sandstone with Bouma sequences and graded bedding on the suprafan (Lin et al., 1991). According to Lin et al. (1991) carbonate apron deposits of the Kelimoli consist of massive breccia of proximal debris flow deposits, graded conglomerate locally showing imbrication structures formed from fluid-rich flow, and pebbly grainstone with large-scale flutes, graded bedding, parallel laminations and cross-bedding. The lack of lenticular channel-fill and sandstone at XLF and YXT, in conjunction with the presence of massive breccia, imbricated conglomerate, and cross-bedded grainstone indicate that the localities of this study are consistent with the carbonate apron depositional model.

Carbonate Apron Depositional Model

The major difference between submarine fans and carbonate aprons is that submarine fans are point-sourced and contain channel deposits on fans, whereas carbonate aprons are line-sourced and exhibit sheet-like flow of sediment (Fig. 7) (Mullins and Cook, 1986). While the facies at each of these environments are similar, their stratigraphic evolution differs, and they are most obviously distinguished by the presence or absence of deeply incised narrow channels, which are only present in submarine fans (Mullins and Cook, 1986). XLF and YXT both lack evidence of narrow incised channels; therefore sediment at these localities was likely deposited on a carbonate apron.

In slope apron models, an extensive blanketlike sheet of shallow-water debris is shed from a platform margin into a basin (Mullins and Cook, 1986). This sheet of sediment is

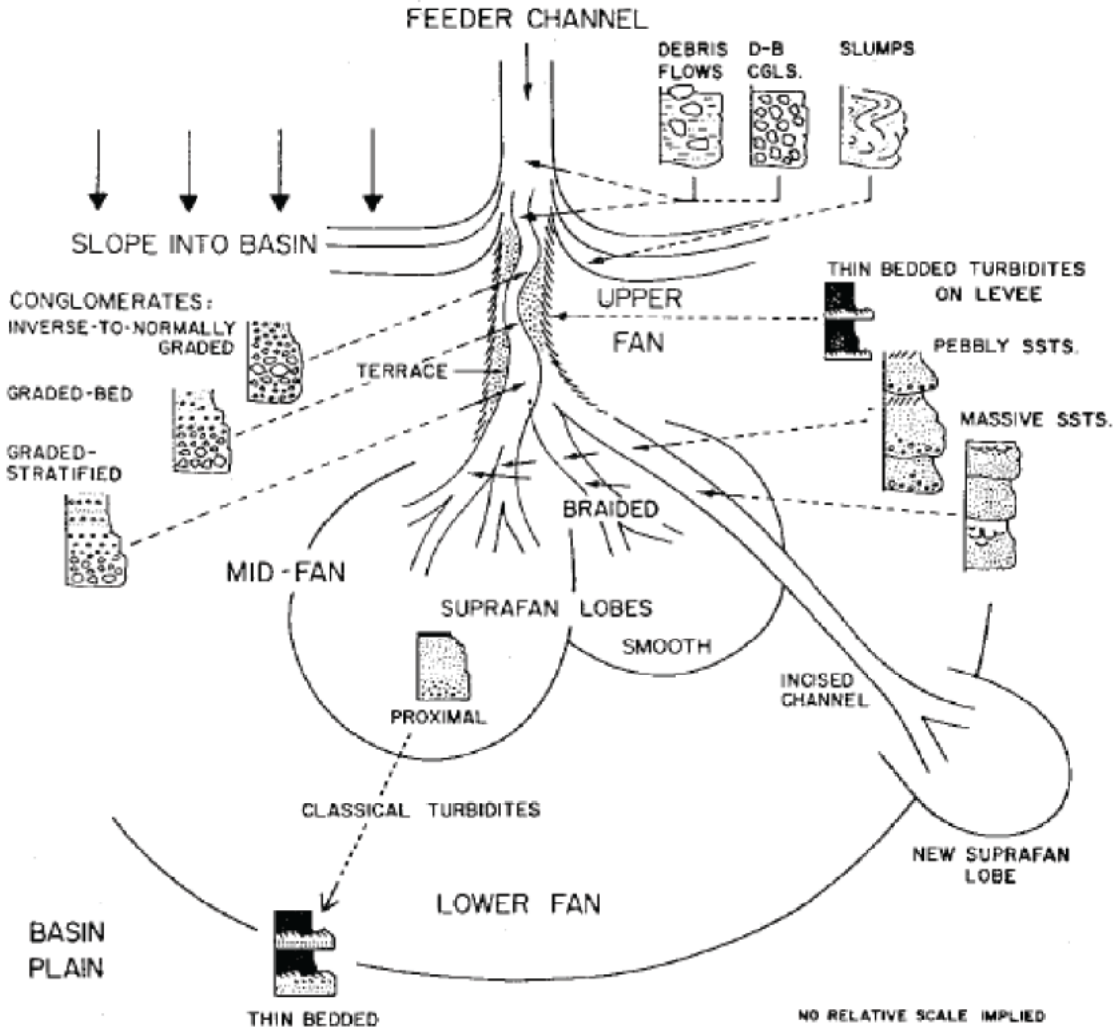

Figure 7. Submarine fan depositional model adapted from Mullins and Cook (1986) with facies associations.

created by many small, closely spaced upper slope submarine canyons, which collectively act as a line source for down-slope transportation of coarse sediment (Mullins and Cook, 1986). The downgoing material is either deposited on the upper slope, or bypasses the upper slope and is resedimented with pelagic sediment by sediment gravity flows, slumps, and slides towards the toe of the apron (Fig. 8) (Tucker and Wright, 1990). Morphologically, a carbonate apron is a relatively smooth surface that gently dips basinward (0.5°-2°) (Mullins and Cook, 1986).

Facies Associations

The facies present in a carbonate apron are subdivided into four facies associations; upper slope, inner apron, outer apron, and basin plain. The upper slope is characterized by hemipelagic and pelagic sediment, the inner apron is dominated by mud-supported conglomerate and megabreccia with some clast-supported conglomerate, the inner apron is characterized by clast-supperted conglomerate with some thin bedded slumps and megabreccia, the outer apron is characterized by thick beds of clast-supported conglomerate that transition to mud-supported megabreccia, and the basin plain exhibits peri-platform or pelagic oozes (Mullins and Cook, 1986).

Lithofacies at XLF are consistent with an outer apron depositional setting. More specifically, the textural variations in the two breccia beds at XLF record variations in flow state, such as what is expected in the outer apron (Mullins and Cook, 1986). Textural patterns are expected to vary as flows progress basinward from matrix-supported to clast-supported fabrics as a result of the progressive removal of matrix and

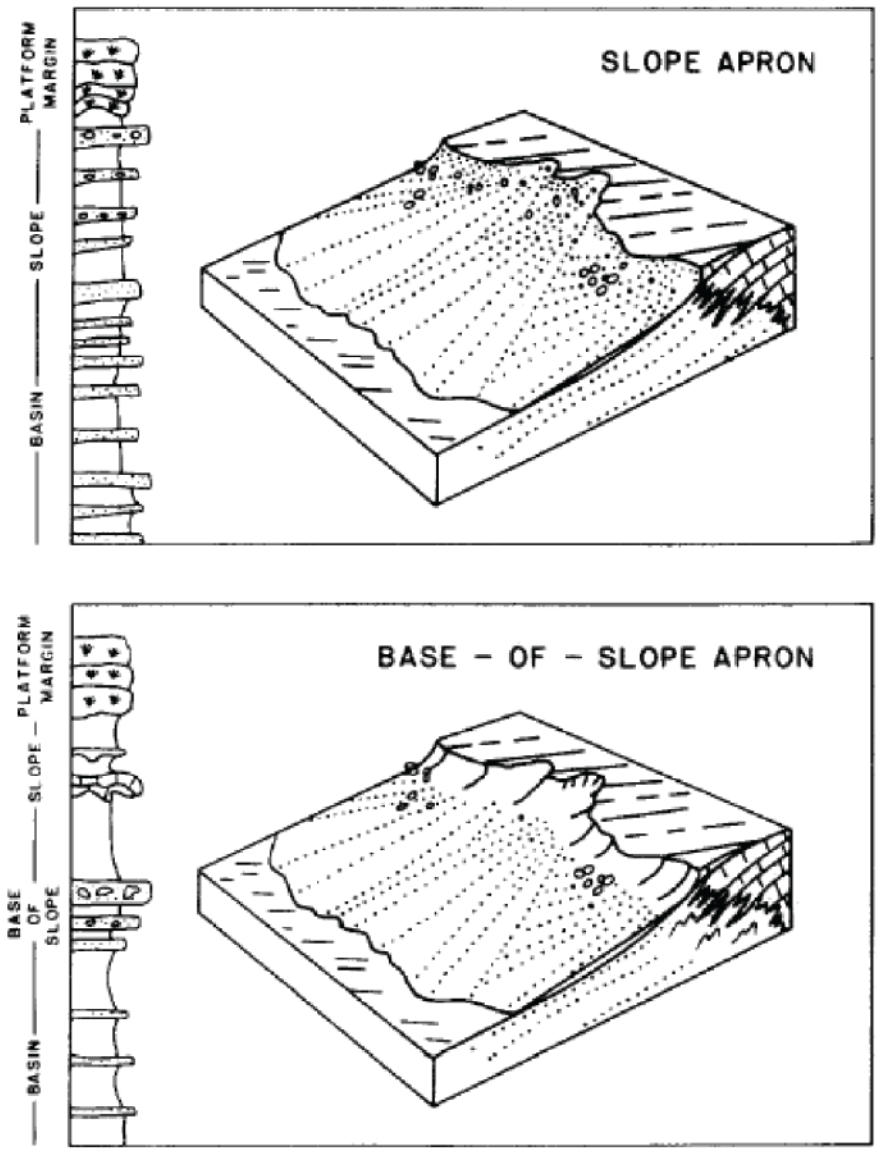

Figure 8. Carbonate apron depositional models. In the slope apron model, facies transition continuously from toe to top of slope. In the base-of-slope apron model, sediment bypasses the upper slope via debris flow or slumping processes, and the majority of sediment accumulates at the toe of the slope (from Mullins and Cook, 1986).

addition of ambient water via turbulence at the top of the flow as it travels downhill (Fig. 9) (Mullins and Cook, 1986).

YXT potentially contains a deeper water succession than XLF, as indicated by the larger percentage of black shale in the upper Kelimoli Formation. It also lacks deformed beds, suggesting that it was deposited on a lower sloping surface, potentially in an area with lower accumulation rates since higher accumulation rates are generally linked to greater probability of slope failure (Mullins and Cook, 1986). These observations suggest that the YXT section was deposited on the basin plain part of the slope apron (Mullins and Cook, 1986).

The biostratigraphic and chemostratigraphic data, which will be discussed in following sections, suggest that there is considerable overlap in age between the YXT and XLF sections, and thus the discrepancy in the thickness of the Kelimoli Formation at XLF (185 m) and YXT (70 m) can be explained by differences in accumulation rates. Their degree of condensation may reflect their relative positions on the carbonate slope apron at the time of deposition. Specifically, XLF is possibly thicker because the facies relationships, particularly the abundance of slump features, suggest that this section was deposited on a more proximal part of the apron, closer to the sediment source. In comparison, YXT was likely located on the basin plain, more distal to the sediment source, based on the absence of slumps and abundance of the black shale facies. Additionally, YXT is west of XLF, indicating that the slope apron thinned in an east to west direction. This is consistent with the paleocurrent direction calculated from clast imbrication data taken from the XLF breccia bed at 174.97 m, which indicates a westward direction of paleoflow. These findings are consistent with Lin et al. (1991),

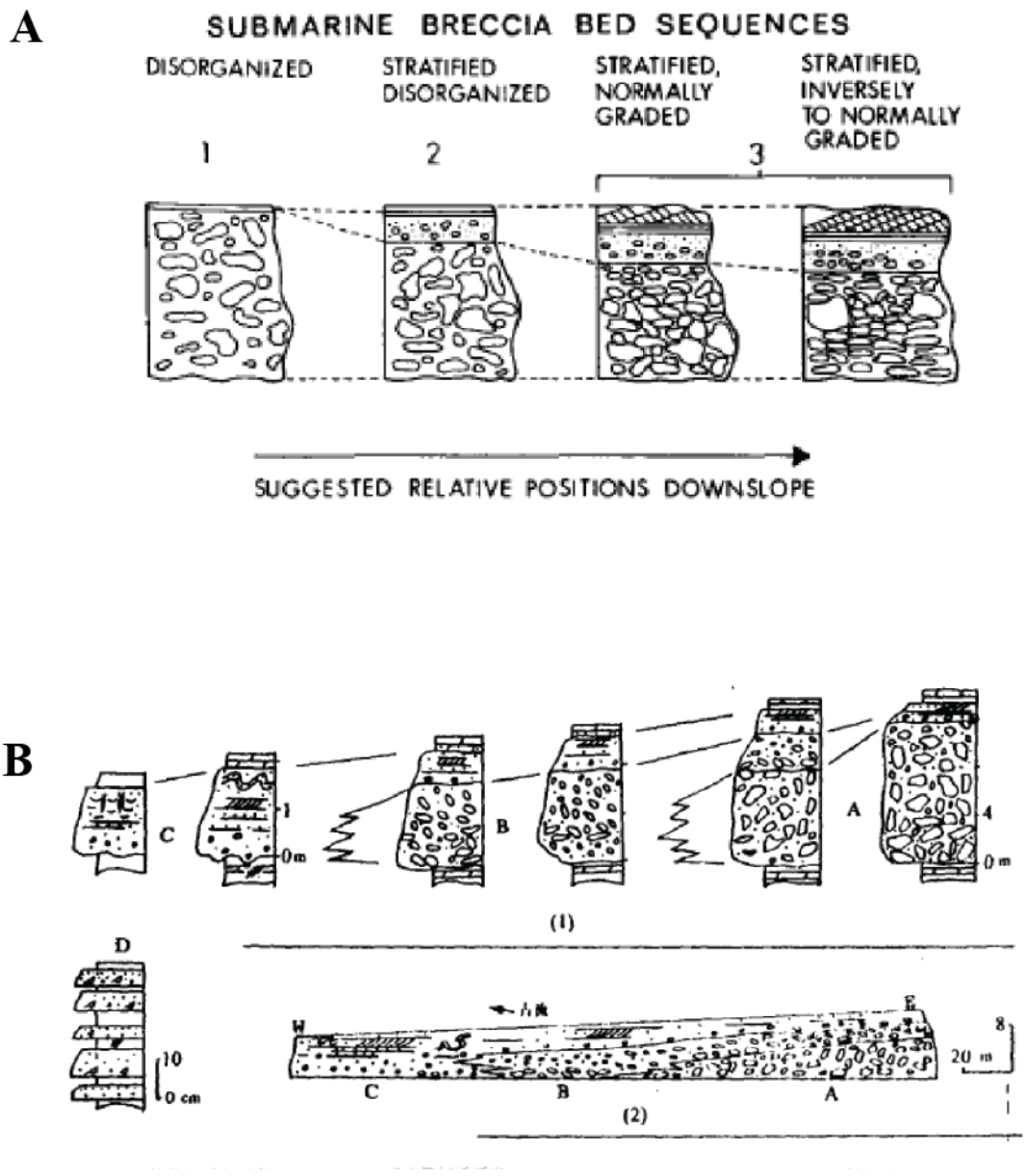

Figure 9. (A) Downslope textural variation in a two-component carboante sediment gravity flow and overriding turbidity current (from Mullins and Cook, 1986); (B) Observed textural variation in debris flows of the Kelimoli Formation (from Lin et al., 1991).

who suggest that the Kelimoli Formation in Inner Mongolia was deposited on the eastern margin of the Helan Aulacogen on a westward-sloping carbonate apron.

Downhill direction inferred from the folded beds (Fig. 5) is southeast, which contradicts the downhill direction inferred from the clast imbrication paleocurrent data. These data were obtained from 12 fold hinges from three different beds at stratigraphic heights between 100 m and 129 m, with as many as four hinge measurements obtained from folds within a single bed. It is possible that the downhill direction at the time of deposition was locally southeast. For example, these folds may have formed on the limbs of ridges parallel to a downward slope, and approximately perpendicular to the overall slope's downhill direction. It is also possible that the folds did not form with their hinge lines parallel to the slope due to physical properties of the sediment, and instead behaved irregularly, or that these measurements do not accurately represent the geometric orientations for the entire section due to insufficient number of samples.

Helan Aulacogen

The Helan Aulacogen formed during the Mesoproterozoic as a failed third arm relative to the Qinling and Qilian rifts, developing in response to long-term convergence of the Qilian block and adjacent Alashan block, and the dextral shearing of the Baoji–Quingtonxia deep fault (Lin et al., 1991; Sun et al., 1983). The Helan Aulacogen extends ~300 km NNE from the Qilian block into the Huabei Platform (Lin et al., 1991). It was filled with approximately 3 km of deep-water deposits from the middle Cambrian through Middle Ordovician, with gravity flow deposits in the basin deposited on the western and eastern marginal slopes during the Middle Ordovician (Lin et al., 1991). More

specifically, submarine fan deposits line the western margin while carbonate apron deposits line the eastern margin, which was adjacent to the epeiric North China Platform (Lin et al., 1991). Facies associations at YXT and XLF are consistent with deposition along the eastern margin of the Helan Aulacogen.

BIOSTRATIGRAPHY

Results

YXT

Wang et al. (2013) provide biostratigraphic data for section YXT, which they refer as their Daishimen locality. Wang et al. (2013) indicate that fauna in the top of the Zhuozhishan Formation, and the lower 43 m of the Kelimoli Formation below the dominant lithology change to shale, correspond to the middle Darwillian *Histiodella kristinae* Zone, such as at the well-known Table Head Formation of western Newfoundland, Canada (Fig. 10) (Wang et al., 2013; Stouge, 1984). However, the upper boundary of this zone is undefined at YXT (Wang et al., 2013). There were no conodont fauna recovered from the graptolitic black shale of the upper Kelimoli Formation, and the overlying Wulalike Formation contains fauna of the early Sandbian *Pygodus anserinus* Baltoscandian Zone (Wang et al., 2013).

XLF

Dr. Steven Leslie of James Madison University analyzed the conodonts from XLF, and preliminarily assigned a sample from 40.13 m to the *Pygodus lunnensis* Zone. However, additional analysis of this sample is needed to confirm this assignment. Dr. Leslie also confidently assigned a sample at 59.8 m to *Pygodus anitae*. Both of these are early Darriwilian Baltoscandian zones (Fig. 10).

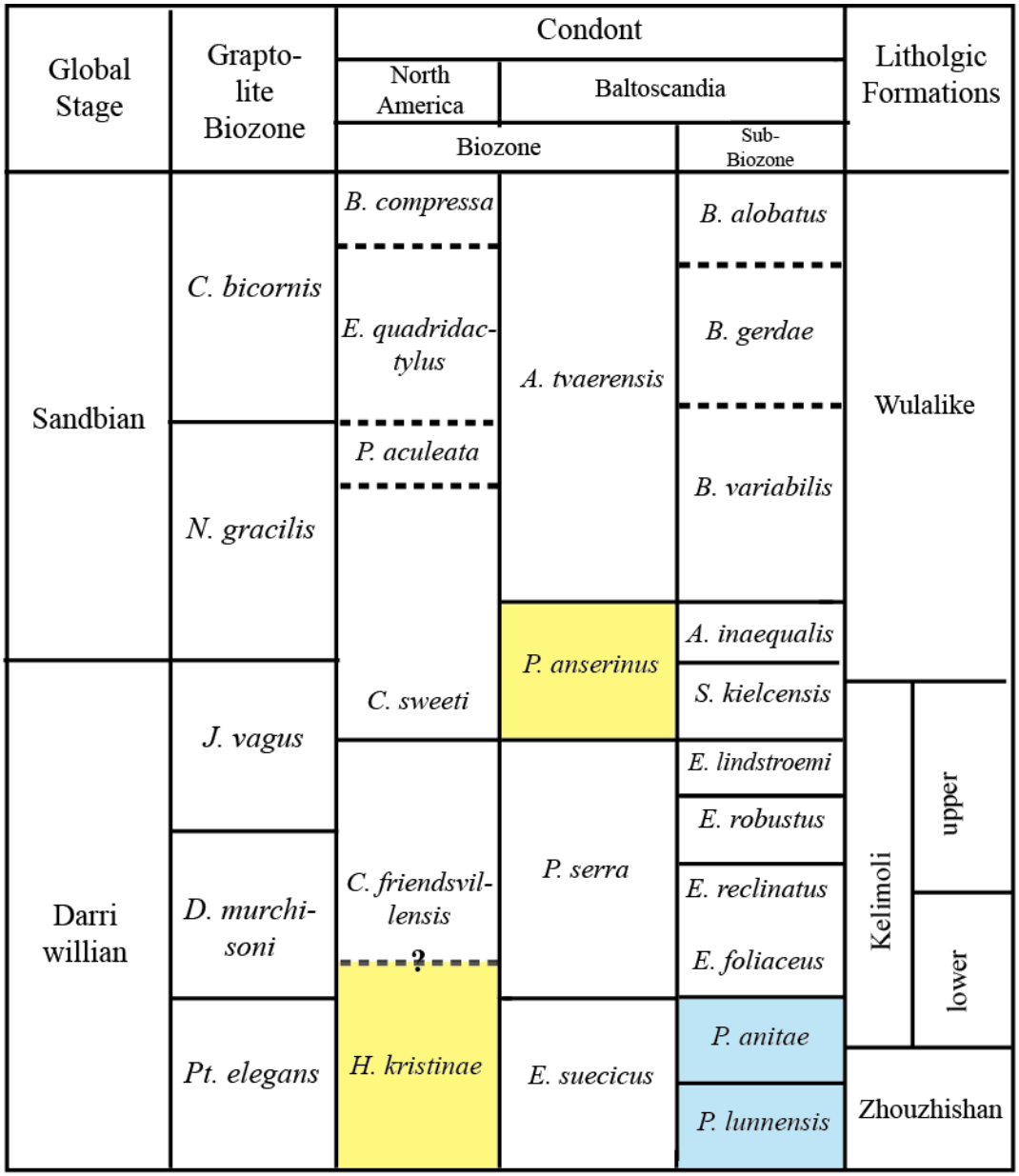

Figure 10. Adapted from Wang et al. (2013) fig. 16. Zones present at YXT are highlighted in yellow, and zones present at XLF are highlighted in blue.

Interpretations

YXT

The *P. lunnensis* and *P. anitae* Baltoscandian Subzones identified at 40.13 m and 59.8 m at XLF, respectively, lie within the North American *H. kristinae* Zone, which is recorded in the lower Kelimoli Formation and the uppermost Zhuozhishan Formation at YXT (Fig. 10) (Wang et al., 2013). However, the boundaries of the Baltoscandian *H. kristinae* Subzone are unknown at YXT, and the presence of *P. lunnensis* at 40.13 m in XLF is uncertain. These factors make biostratigraphic correlations between YXT and XLF difficult.

XLF

P. anitae Subzone is certainly present at 59.8 m in XLF, and this subzone at least partially overlaps in age with the *H. kristinae* Zone (Wang et al., 2013). There is not enough information to assign specific ages to some stratigraphic positions at both sections, preventing precise age correlations between sections based on conodonts alone. However, the boundary between graptolite biozones *Pt. elegans* and *D. murchisoni* lies at 25 m in YXT, and this boundary roughly corresponds with the top of the *P. anitae* Subzone (Fig. 10). There is no conodont information stratigraphically higher than 59.8 m at XLF as these samples are pending analysis. Therefore, assuming that 59.8 m represents the top of the *P. anitae* Subzone, then 25 m at YXT is the same age as 59.8 m at XLF. This hypothesis can be tested in the future with conodont and graptolite sampling above 59.8 m at XLF.

There are four possible interpretations based on biostratigrahpic results from the XLF sample at 40.13 m: (1) the conodonts at 40.13 m belong to the *P. lunnensis* Subzone (Fig. 11); (2) the conodont sample is *P. lunnensis*, but is present in a highly condensed section; (3) the conodont sample is not *P. lunnensis* and instead is *P. anitae* (Fig. 12); (4) the conodont sample is not *P. lunnensis* and instead belongs to a zone that places 40.13 m below the *H. kristinae* Zone.

Interpretation 1 indicates that 40.13 m corresponds with the *H. kristinae* Zone at YXT, and falls somewhere within the lower Kelimoli Formation or upper Zhuozhishan Formation. This interpretation fails to explain the difference in thickness of the Kelimoli Formation (below the black shale) between XLF (~185 m) and YXT (~67 m). Interpretation 2 suggests that the Kelimoli Formation at both localities was deposited in the same amount of time, indicating that YXT is ~5 times condensed compared to XLF (if the first 34 m of YXT are equivalent to all 170.48 m of the XLF section) Both of these interpretations require a depositional model to explain the difference in thickness of the Kelimoli Formation between localities.

Interpretation 3 would require that 40.13 m in XLF belongs to *P. anitae*, indicating that 40.13 m in XLF corresponds to the *H. kristinae* zone at YXT, but to a stratigraphically higher position relative to interpretation 1 because *P. anitae* Zone is younger than the *P. lunnensis* Zone (Fig. 10). Interpretation 4 suggests that 40.13 m is older than the *H. kristinae* Zone in YXT, and would correspond to the lower Zhuozhishan Formation (assuming that the base of the *H. kristinae* Zone is in the Zhuozhishan Formation). This would mean that much of the fine-grained mixed facies of the lower part of XLF would be equivalent in age to the cliff-weathering Zhuozhishan Formation.

This interpretation would probably also require an unconformity at XLF that eroded rocks containing *P. lunnensis*.

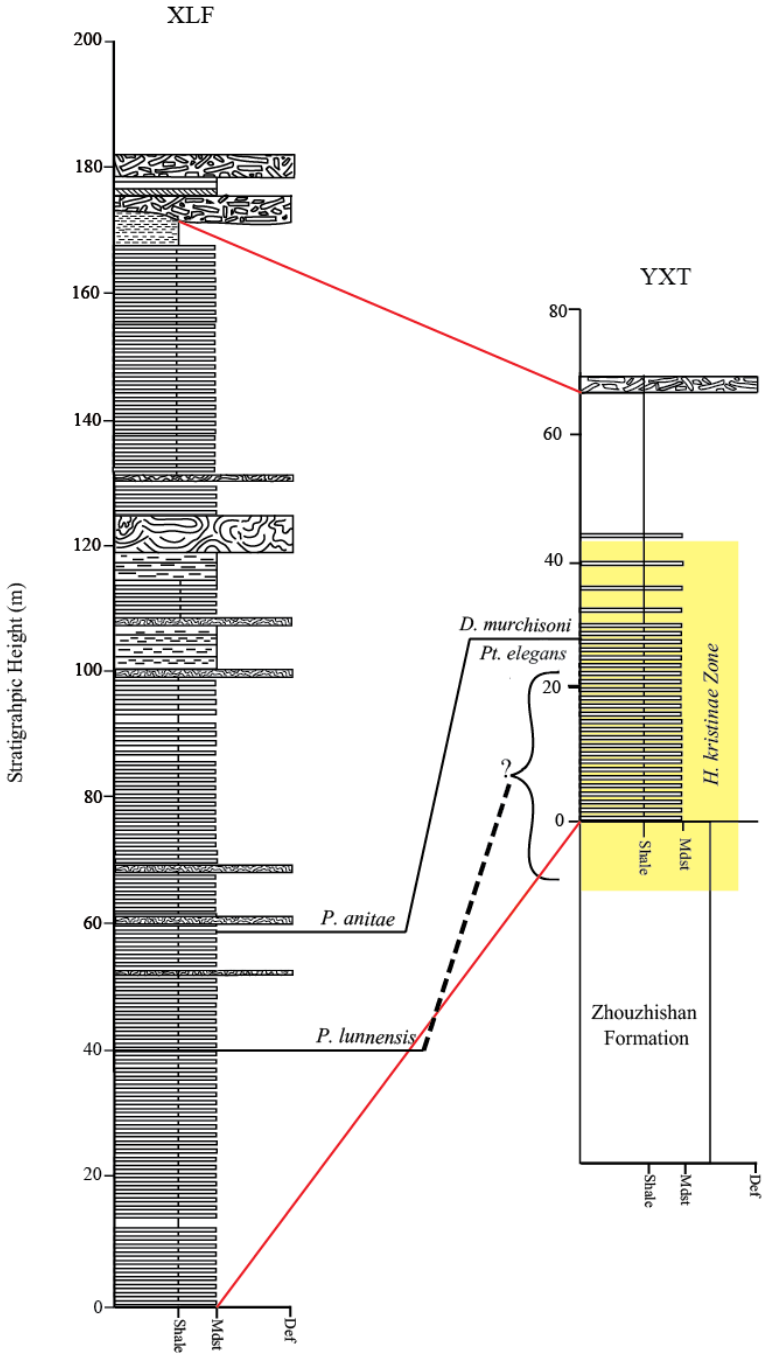

Figure 11. Generalized stratigraphic columns for XLF and YXT showing relative thickness and stratigrahpic correlation based on biostratigrahpic interpretations 1 and 2. The *H. kristinae* biozone at YXT is highlighted in yellow, and extends below the base of the Klimoli Formation, into the Zhoushizhan Formation (massive carbonate). XLF 59.8 m represents the top of *P. anitae* which also occurs at 25 m in YXT. Interpretation 1 is depicted by the red lines, showing that the base of the Klimoli Formation and top of the black shale in both sections are the same age. Therefore, YXT is highly condensed relative to XLF. In interpretation 2, XLF 40.13 m corresponds to an unidentifiable position within the *H. kristinae* zone at YXT.

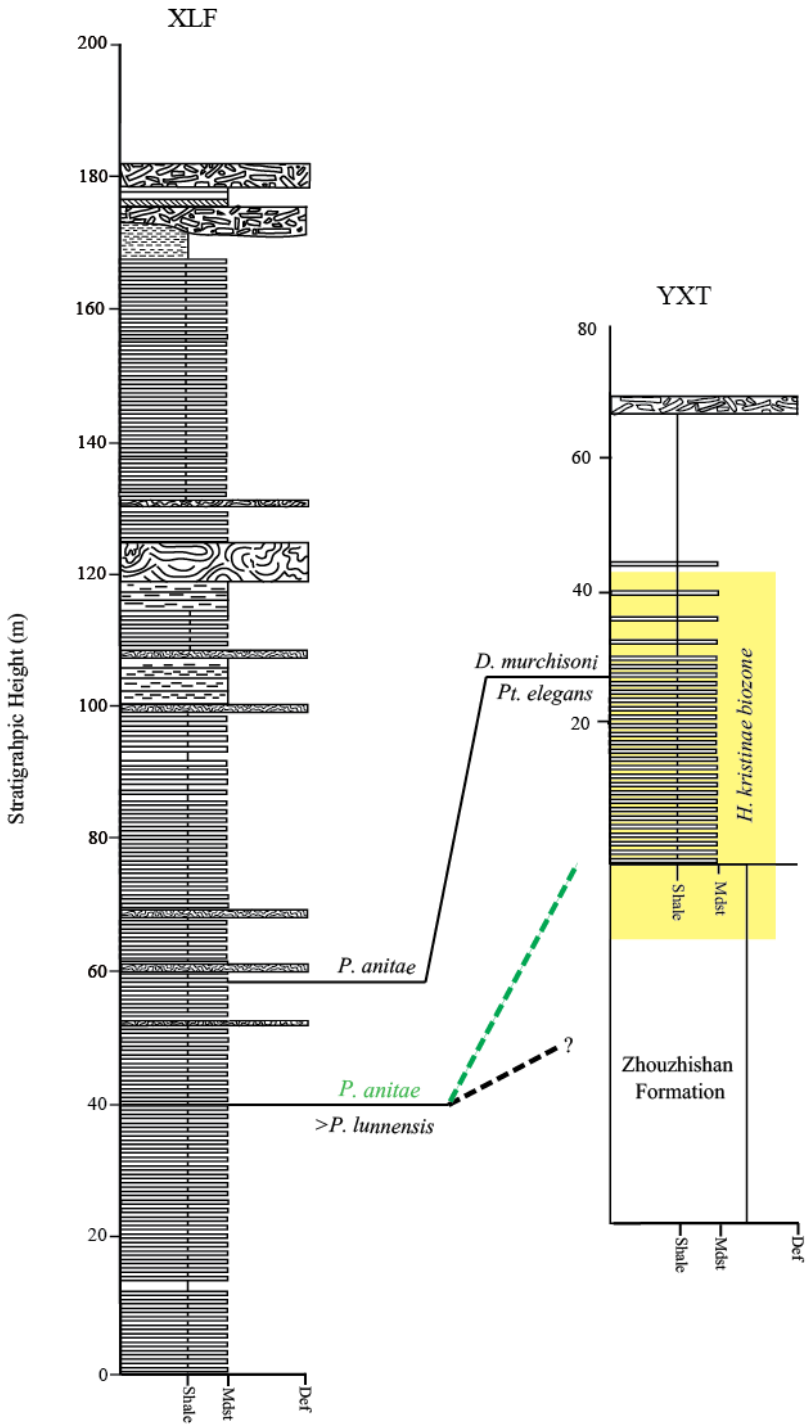

Figure 12. Generalized stratigraphic columns for XLF and YXT showing relative thickness and stratigrahpic correlation for interpretations 3 and 4. Interpretation 3 is depicted by the green dashed line and shows 40.13 m in XLF as *P. anitae*, which corresponds relatively lower in the *H. kristinae* zone at YXT compared to interpretations 1 and 2. Interpretation 4 is depicted by the black line, which shows that 40.13 m at XLF belongs to a zone that is older than *P. lunnensis*, and correlates below the *H. kristinae* Zone at YXT.

CHEMOSTRATIGRAPHY

Results

YXT

The YXT $\delta^{13}C$ curve is comprised of 172 data points plotted over 48.3 m of section (Fig. 13). Values at the base of the section range from ~-2.0‰ to ~0.2‰ for the first ~5 m with the exception of one outlying data point of ~-4‰ at ~4 m. Values become more positive from ~5 m to ~12 m, and then remain in the ~0.2‰ to ~-1.0‰ range until ~35 m, where there are fewer data due to lithological constraints. Lower values begin occurring at approximately 35 m, beginning with values at ~-1.2‰ at 35 m that drift to ~-3.5‰ by 48.3 m and exhibit oscillations that range from 1‰ to 3‰.

XLF

The XLF $\delta^{13}C$ curve is comprised of 266 data points plotted over 170.48 m of section (Fig. 14). This section lacks any excursions and exhibits very little, if any, change in $\delta^{13}C$ values, which generally lie between 0‰ and 1‰ for the entire section. This general trend is superimposed by high frequency variability of 0.2‰ to 0.7‰, although oscillations are more pronounced at approximately 73 m, where variability is as high as 2‰. After 140 m, the values decrease, although the $\delta^{13}C$ curve has fewer data points due to lithological constraints.

Interpretations

YXT

Strong biostratigraphic control places the lower Kelimoli Formation at YXT in the *H. kristinae* Zone, which belongs to the Dw2 and Dw3 stage slices defined by Bergstrom et al. (2009). These stage slices broadly correspond with the peak values and falling limb of

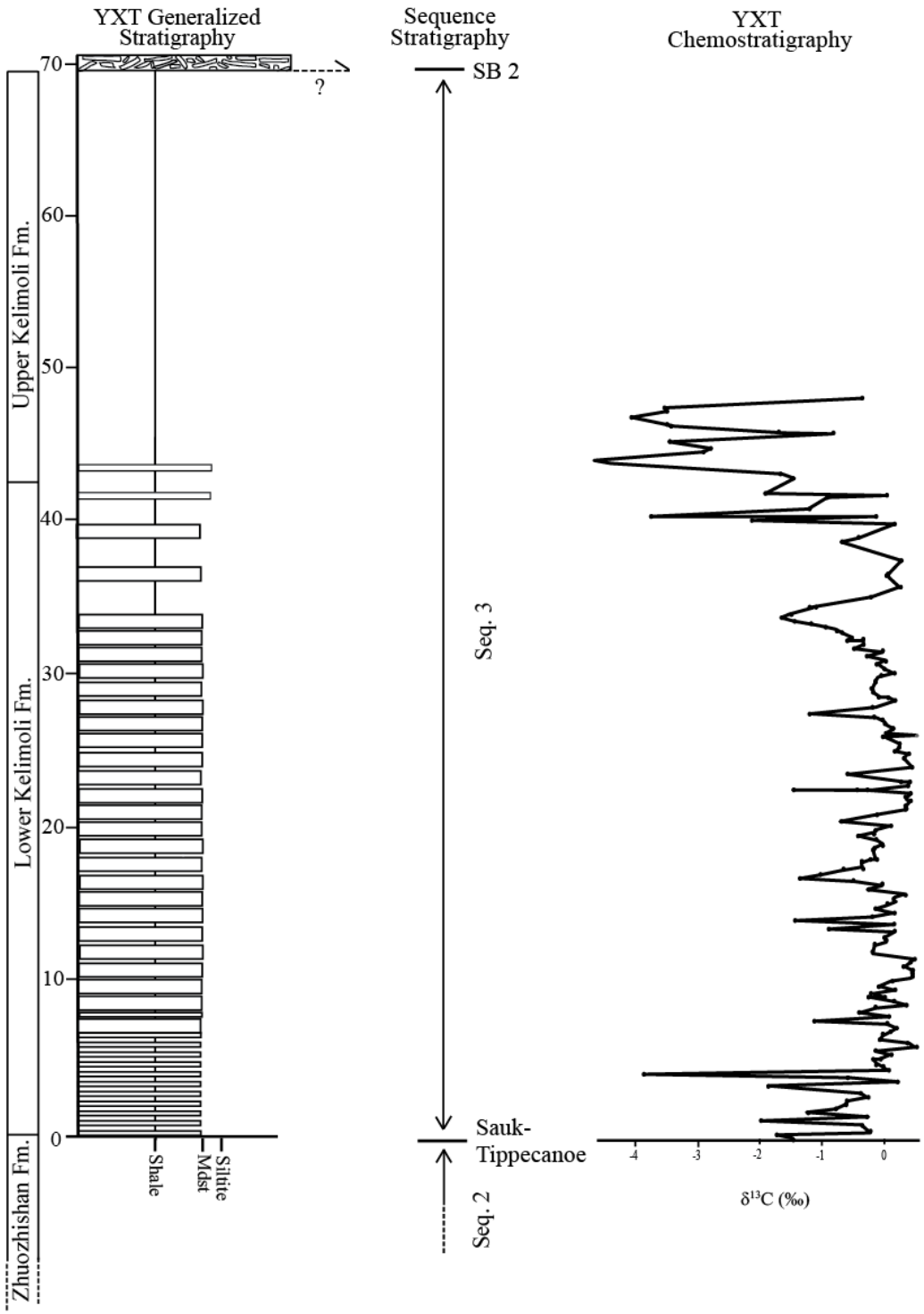

Figure 13. Simplified stratigrahpic column for YXT (left) with chemostratigraphic data for corresponding stratigraphy (right).

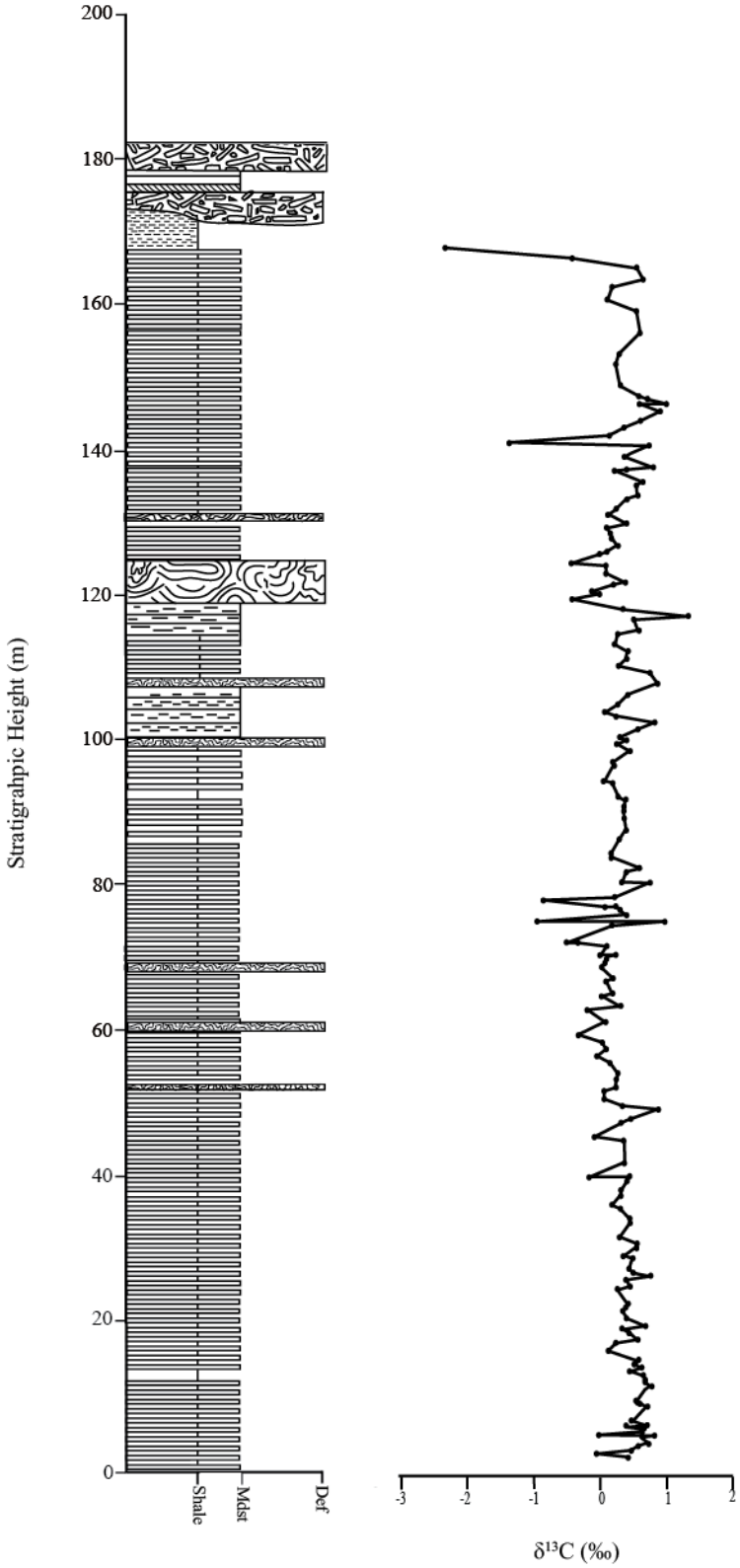

Figure 14. Simplified stratigrahpic column for XLF (left) plotted with corresponding chemostratigrahpic data (right).

the Mid-Darriwilian Carbon Isotope Excursion (MDICE), respectively (Fig. 15). The negative drift in $\delta^{13}C$ values beginning at ~40 m continuing through the top of YXT are consistent with the descending limb of MDICE.

XLF

The XLF biostratigraphic results were not conclusive. However, they provide a minimum age for the section; *P. anitae* (59.8 m) lies below the base of *P. serra* which corresponds to stage slice Dw3 within the Darriwilian (Fig. 10, Fig. 15). Therefore, the minimum age of 59.8 m at XLF corresponds with Dw3. According to Schmitz et al. (2010), strata from several different regions globally that lie immediately below the *P. serra* biozone exhibit peak $\delta^{13}C$ values for the Mid-Darriwilian Carbon Isotope Excursion (MDICE), which is characterized by $\delta^{13}C$ values that are ~1‰ higher than the $\delta^{13}C$ values in slightly older and younger stratigraphic intervals (Fig. 16) (Schmitz et al., 2010). The general pattern of XLF chemostratigrahpic data, which oscillate between 0‰ and 1‰ without any major excursions, matches the general pattern of age equivalent chemostratigraphic data from Estonia, which comprise part of MDICE (Schmitz et al., 2010). The absolute values of $\delta^{13}C$ at XLF are approximately 1‰ lower than age equivalent data from Estonia, although absolute values typically vary between sections in general in the rock record. Chemostratigraphic data for *E. suecicus* are absent from sections in Sweden and Hunan, China (South China) due stratigraphic gaps. I suggest that the data at XLF represents MDICE in the NCB based on biostratgraphic and chemostratigraphic correlation. Additionally, this interpretation supports biostratigraphic interpretations 1 and 2 because *E. suecicus* contains the boundary between *P. anitae* and *P. lunnensis*.

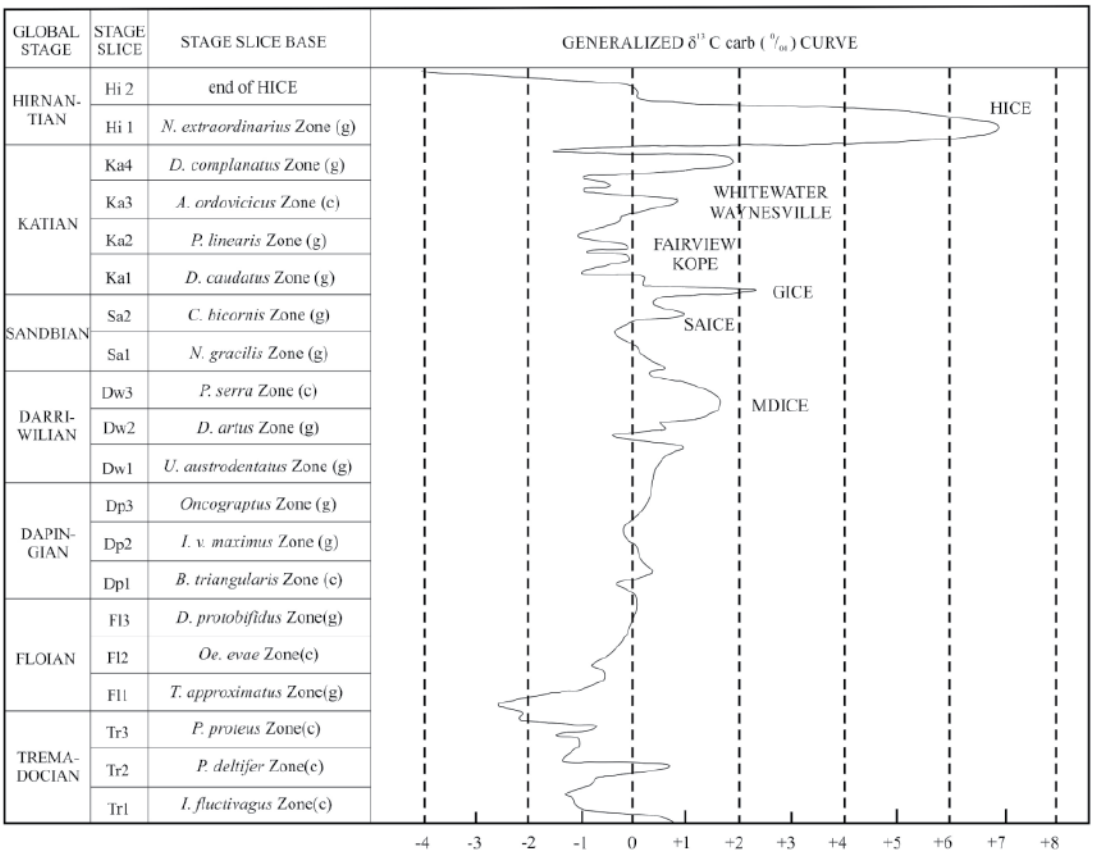

Figure 15. Generalized $\delta^{13}C$ curve and corresponding global stages, and biostratigraphy (c= conodont, g=graptolite) (adapted from Albanesi et al., 2013).

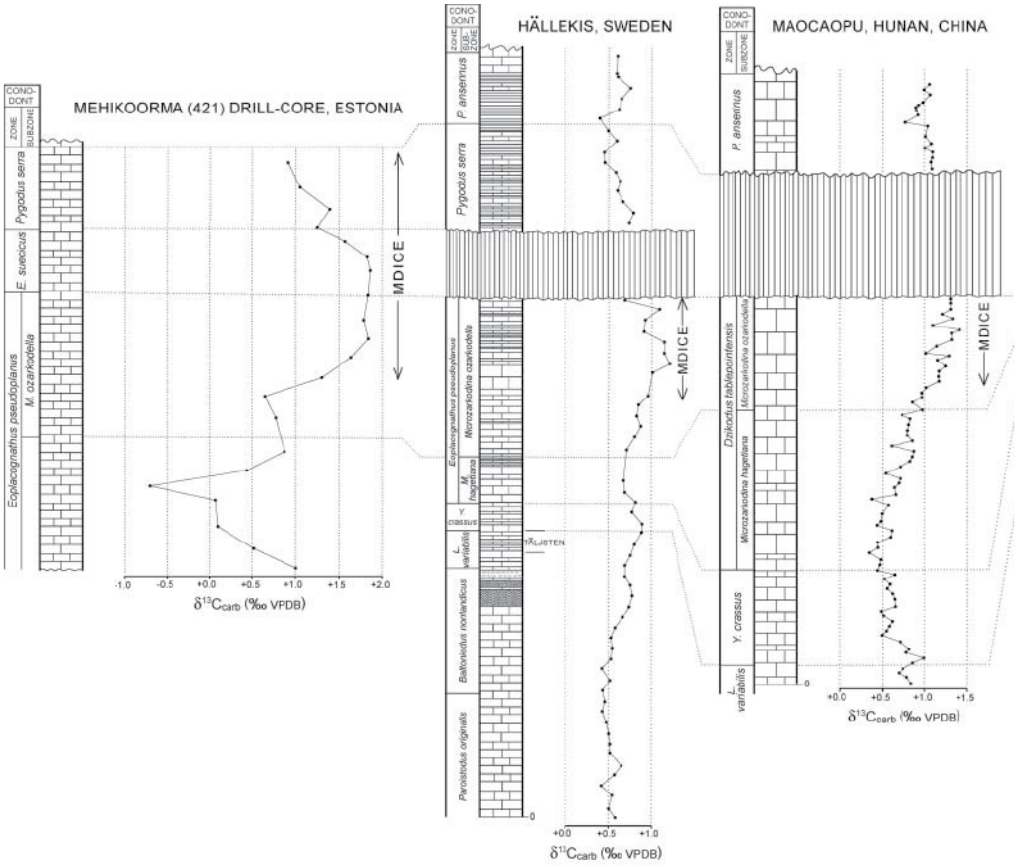

Figure 16. Global correlation of MDCIE. Vertical shading represents nondeposition and concides with the *E. suecicus* zone in Sweden and South China (from Schmitz et al., 2010).

Relative Ages of YXT and XLF

XLF lacks the decrease in $\delta^{13}C$ present at the top of YXT. These values are likely missing from XLF because strata containing this record slumped away, or erosion at the base of the breccia units removed such strata. If so, the entirety of XLF might correspond with 0–40 m at YXT, representing peak MDICE values, while 40–50 m at YXT are marginally younger than the top of XLF and represent the beginning of the MDICE descending limb (Fig. 17). This interpretation supports biostratigraphic interpretation 2, suggesting that YXT is 5 times more condensed than XLF.

Other Regional Evidence for MDICE

Previous research by Myrow et al. (*in press*) found *H. holodentata* in the lower part of their Subaiyingou section (SBG) of the Sandaokan Formation (lowest Middle Ordovician) in Inner Mongolia. They interpret chemostratigraphic data from SBG as belonging to the rising limb of MDICE. This finding complements chemostratigraphic interpretations for XLF and YXT, which represent the peak and falling limbs of MDICE, respectively. Therefore, the only missing part of MDICE would be found in outcrops of the upper Sandaokan Formation and full Zhuozhishan Formation (between the Sandaokan and Kelimoli formations, Fig. 2) in Inner Mongolia (Fig. 18).

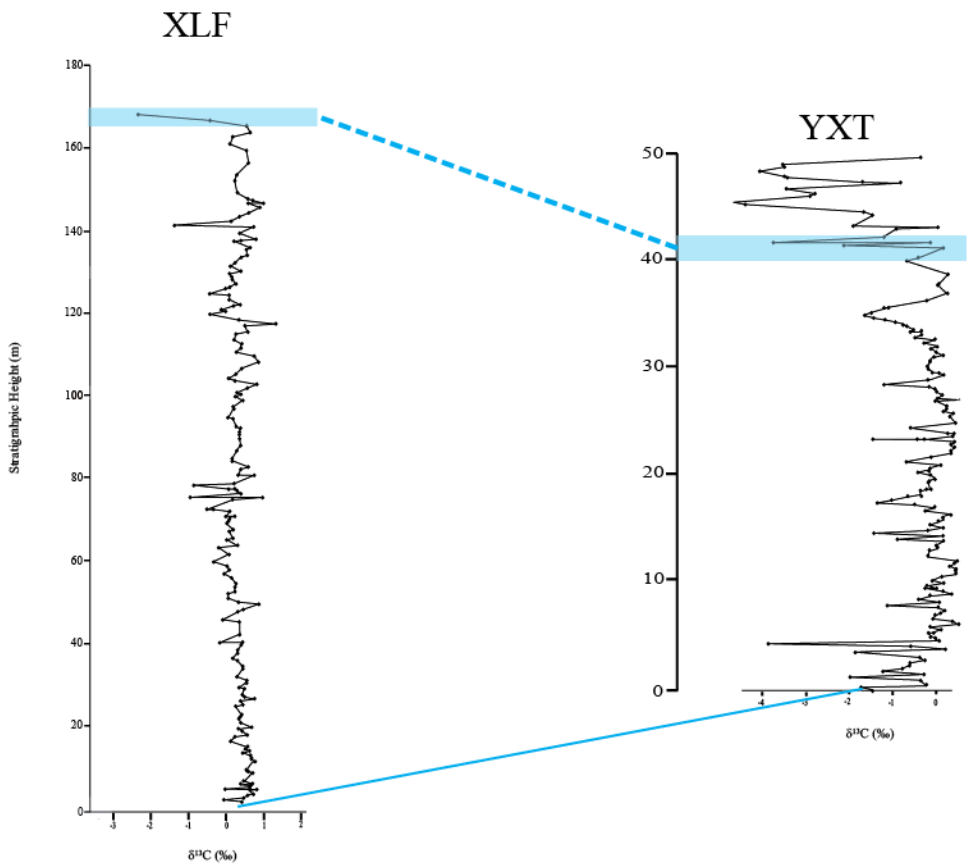

Figure 17. Age relationship between XLF and YXT inferred from chemostratigraphy. The blue boxes indicate zones containing (YXT) or expected to contain (XLF) negative drift characteristic of the descending limb of MDICE.

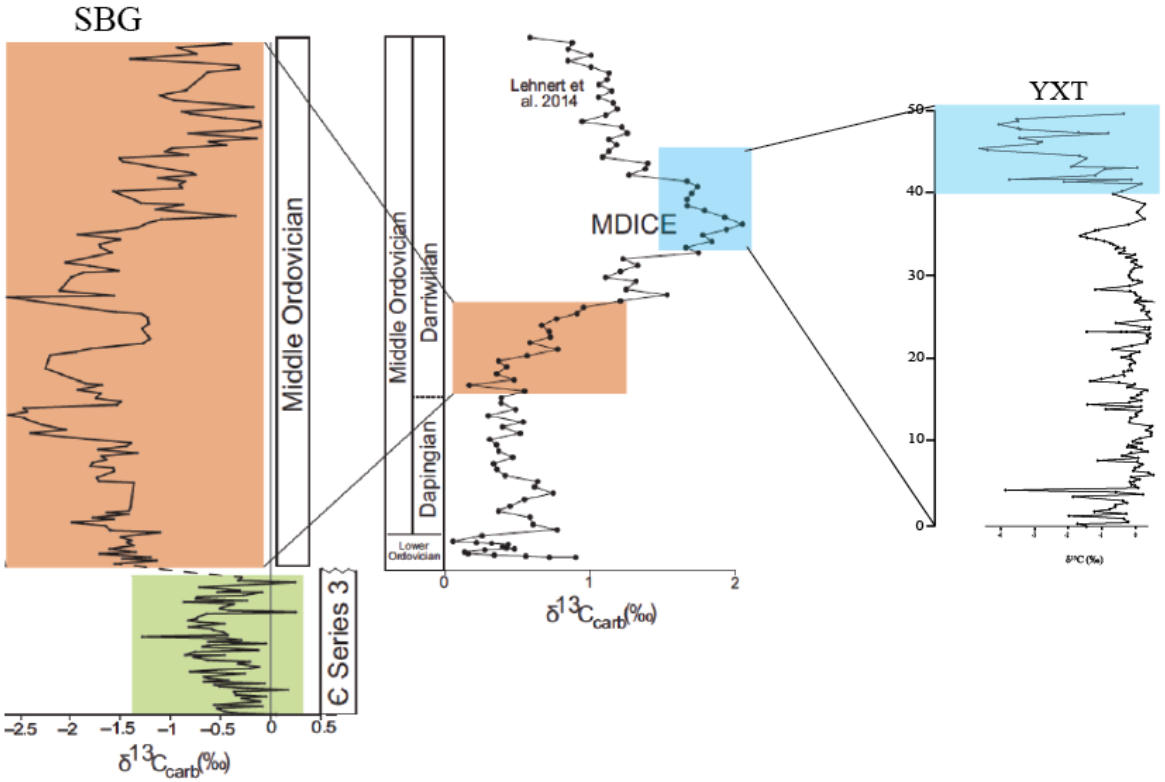

Figure 18. Chemostratigrahpic correlation of SBG (orange boxes), XLF and YXT (blue box) with MDICE (adapted from Myrow et al., *in press*).

DISCUSSION

MDICE

MDICE occurs on several different paleocontinents and is constrained with biostratigraphic data, allowing for global correlation of sections. More specifically, MDICE has been found in the South China paleoplate (Schmitz et al., 2010; Zhang et al., 2010), southern Appalachians (Leslie et al., 2011), northern Appalachians of Newfoundland (Thompson et al., 2012), Argentine Precordillera (Buggisch et al., 2003; Albanesi et al., 2013; Sial et al., 2013), and Baltoscandia (Ainsaar et al., 2004; Meidla et al., 2004; Martma, 2005; Ainsaar et al., 2007, Ainsaar et al., 2010; Kaljo et al., 2007; Calner et al., 2014).

While the cause of MDICE is still debated, integrated biostratigraphic and chemostratigraphic data from several regions throughout the globe indicate that the beginning of the descending limb commonly coincides with significant depositional gaps at the base of the *P. serra* Zone, which are likely associated with eustatic decline during a late phase of the North American Whiterock regressions (Fig. 16) (Schmitz et al., 2010). The Whiterock regressions exposed a large part of the North American craton, resulting in the formation of the Sauk–Tippecanoe megasequence (Schmitz et al., 2010; Finney et al., 2007). The cause of the Whiterock regressions is debated, and may be related to glaciation events in Gondwana (Schmitz et al., 2010).

Implications of Unconformity and MDICE in Inner Mongolia

The lower Kelimoli Formation at YXT belongs to *H. kristinae* and the upper Kelimoli Formation lacks conodonts. However, the upper Kelimoli Formation contains graptolite

fauna of the *D. murchisoni* Zone, and is overlain by the Wulalike Formation, which contains *P. anserinus* fauna. This progression of biozones means that there is a depositional gap between the lower Kelimoli Formation and the Wulalike Formation that corresponds with the *P. serra* Zone.

Chemostratigraphic interpretation 2 suggests that there is missing time at the top of XLF, indicated by the absence of the negative drift in $\delta^{13}C$ that is observed at YXT, while biostratigraphic data indicate a possible stratigraphic gap at the top of YXT. This could mean that the top of MDICE is not observed at XLF and YXT because nondeposition occurred at these localities beginning immediately below the *P. serra* Zone, which chronostratigrahpically corresponds with beginning of the descending limb of MDICE (Schmitz et al., 2010). This is observed in sections in Sweden and South China, which contain incomplete records of MDICE due to nondeposition during *E. suecicus* (equivalent to *H. kristinae*) and *P. serra* zones (Fig. 16) (Edwards and Saltzman, 2014; Schmitz et al., 2010). The geographically widespread period of nondeposition immediately before and during *P. serra* could indicate the presence of a global unconformity that corresponds with a boundary between megasequences.

Proposed Sequence Stratigraphic Framework

Previous sequence stratigraphic research for the NCP identifies two megasquences within Cambrian–Ordovician strata. Megasequence 1 contains nine sequences and lasted ~40 m.y. from the Lower Cambrian to Lower Ordovician, and megasequence 2 contains three sequences and lasted ~30 m.y. from the Middle to Upper Ordovician (Fig. 19) (Meng et

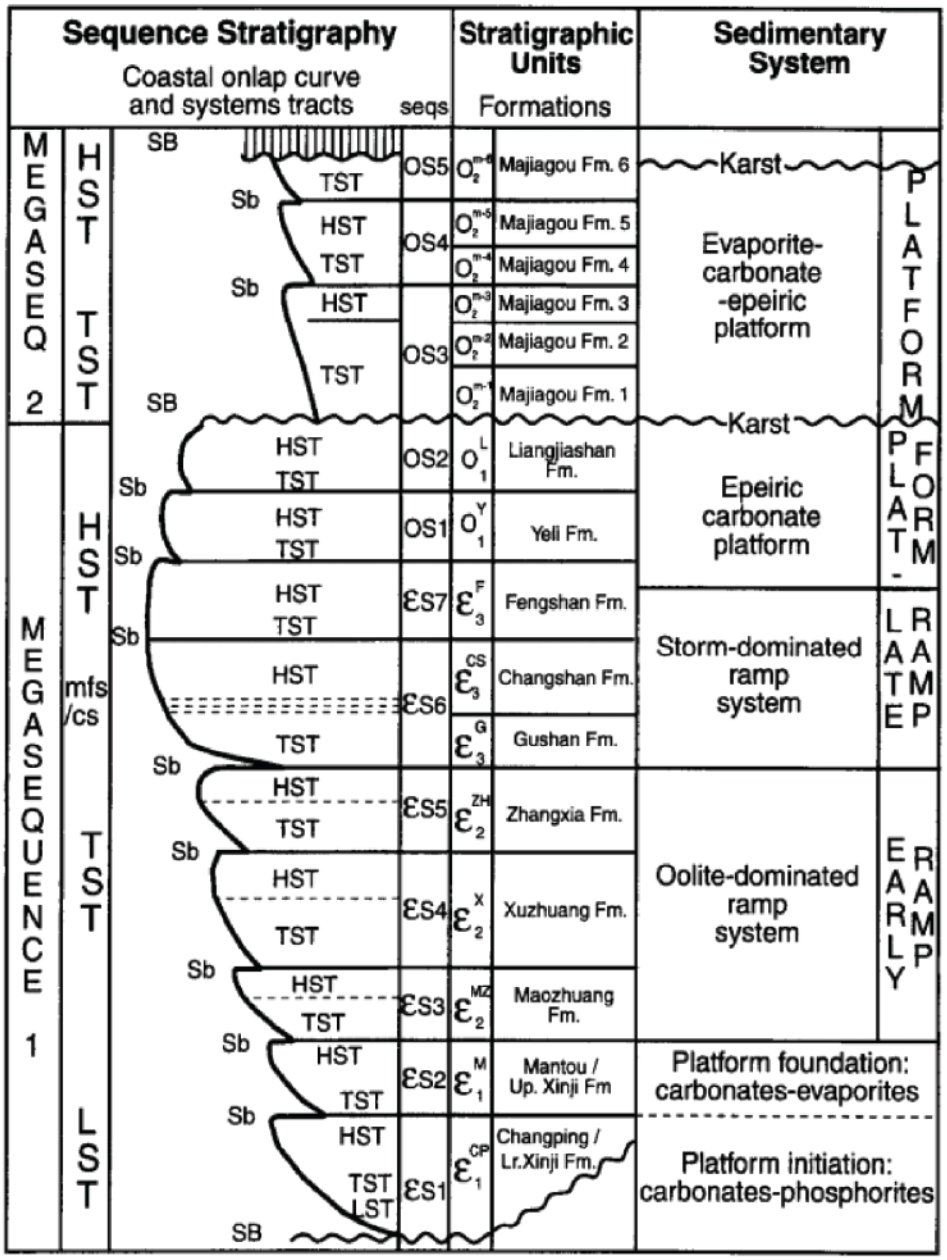

Figure 19. Sequence stratigraphy of the North China Platform according to Meng et al. (1997).

al., 1997). The facies in both megasequences show a long-term rise and fall of sea level, with lower transgressive parts and upper regressive parts. Megasequence 2 is of particular interest to this study because the Kelimoli Formation is Middle Ordovician.

Biostratigraphic control and previous studies of lower Middle Ordovician geology in the NCB allow for the proposal of a sequence stratigraphic framework for the region. In the NCB, Archean basement is unconformably overlain by Paleozioic through Cambrian strata with a disconformity between the Cambrian series 3 Abuqiehai Formation and the overlying upper Middle Ordovician Sandaokan Formation (Myrow et al., *in press*). On the NCP, The boundary between megasequences 1 and 2 (SB1) lies at the base of the Lower Ordovcian Majiagou Formation (Meng et al., 1997). Therefore, SB1 is contained within a disconformity in the NCB at the base of the Sandaokan Formation.

The Sandaokan Formation is overlain by the Zhouzhishan Formation, and the contact between them likely temporally corresponds with the North American Sauk-Tippecanoe megasequence boundary according to biostratigrahpic correlation between strata of the NCB and North America. Correlation of the NCB with North American strata may be useful for future studies that attempt to correlate sea level rise and fall globally. Specifically, the Sauk–Tippecanoe megasequence boundary in west–central Utah corresponds with the *H. holodentata–Phramagodus harrisi* Zone boundary (Ethington et al., 2012). *P. harrisi* is the age equivalent of *E. suecicus* and *H. kristinae* (Bauer, 1989). Therefore, the *H. holodentata–P. harrisi* boundary is equivalent with the *H. holodentata–H. kristinae* boundary (Edwards and Saltzman, 2014 fig. 4). Myrow et al. (*in press*) assigned the base of the Sandaokan Formation in their Suibaiyingou Valley locality

(SBG) in Inner Mongolia to *H. holodentata*, and Wang et al. (2013) indicate that *H. kristinae* is present in the uppermost Zhuozhishan Formation at YXT. The boundary between *H. holodentata* and *H. kristinae* must be found between the base of the Sandaokan and uppermost Zhuozhishan, and likely corresponds with a major lithologic change. Therefore, I hypothesize that the Sauk–Tippecanoe megasequence boundary is located at the base of the Zhuozhishan Formation in Inner Mongolia, the most significant lithologic shift in that interval, and that the Sandaokan Formation corresponds with deposition during sequence 1, and the Zhouzhishan Formation represents deposition during sequence 2. Sequence 3 is contained within the upper part of the Majiagou Formation on the NCP, which also contains the *D. murchisoni-Pt. elegans* graptolite zone boundary. This boundary is also present in the NCB at 25 m in the lower Kelimoli Formation, indicating that the Kelimoli Formation represents deposits of sequence 3, and that the unconformity between the black shale facies of the upper Kelimoli Formation and the overlying Wulalike Formation breccia facies indicated by the absence of *P. serra* zone fauna corresponds with the upper boundary of megasequence 2 (SB2) (Meng et al., 1997).

It is important to note that megasequence 2 is not fully developed in much of China due to tectonic uplift at Middle–Upper Ordovician boundary likely associated with the Caledonian Orogeny (Liu et al., 1997). Therefore it is possible that megasequence 2 is either (1) represented in the NCB in its entirety, and only contains three sequences (Fig. 20), or that (2) megasequence 2 is not fully recorded in the NCB, and Middle Ordovician strata only represent part of the full megasequence (i. e., three of possibly four or more

total sequences) (Fig. 21). However, the presence of black shale, marking the transition from lower to upper Kelimoli Formation, indicates sea level rise, suggesting that second

hypothesis is more likely because the shale likely represent deep water deposition and a transgressive systems tract.

Sedimentological Context for Sequence Stratigraphic Framework

This sequence stratigraphic framework of megasequence 2 for the NCB is put in context of sedimentological and chemostratigraphic data for YXT (Fig. 13). Note that the lower boundary of megasequence 2 (disconformity between Abuqeihai and Sandaokan formations), and sequence 1 (Sandaokan Formation), and the Sauk-Tippecanoe megasequence boundary are not depicted because they are not present at YXT. However, Fig. 13 shows the Zhouzhishan Formation as sequence 2 deposits, the Kelimoli Formation as sequence 3 deposits, and the placement of SB2 at the top of the Kelimoli Formation black shale facies. These interpretations match with observed sedimentology. In particular, water gets progressively deeper from sequence one to three explaining the transition in dominating facies from bioturbaed wackestone and quartz sandstone to shallow water carbonates, and deeper water interbedded mudstone and marl and black shale of the Sandaokan, Zhouzhishan, and Kelimoli formations, respectively (Myrow et al., *in press*). Chemostratigrapy shows that the peak MDICE values and the beginning of the descending limb occur during sequence 3 in the Kelimoli Formation. The unconformity at the top of the Kelimoli Formation in the *P. serra* Zone is globally widespread and may correspond with SB2 in the NCB, but that this megasequenc boundary may be able to be correlated globally (Schmitz et al., 2010). Furthermore, this

megasequence boundary may correspond to the Middle-Upper Ordovician Boundary which is characterized by climatic cooling, which could have changed the depositional environment in the Helan Aulocogen and proximal carbonate shelf, resulting in the deposition of breccia on top of the upper Kelimoli Formation (Ainsaar et al., 2010).

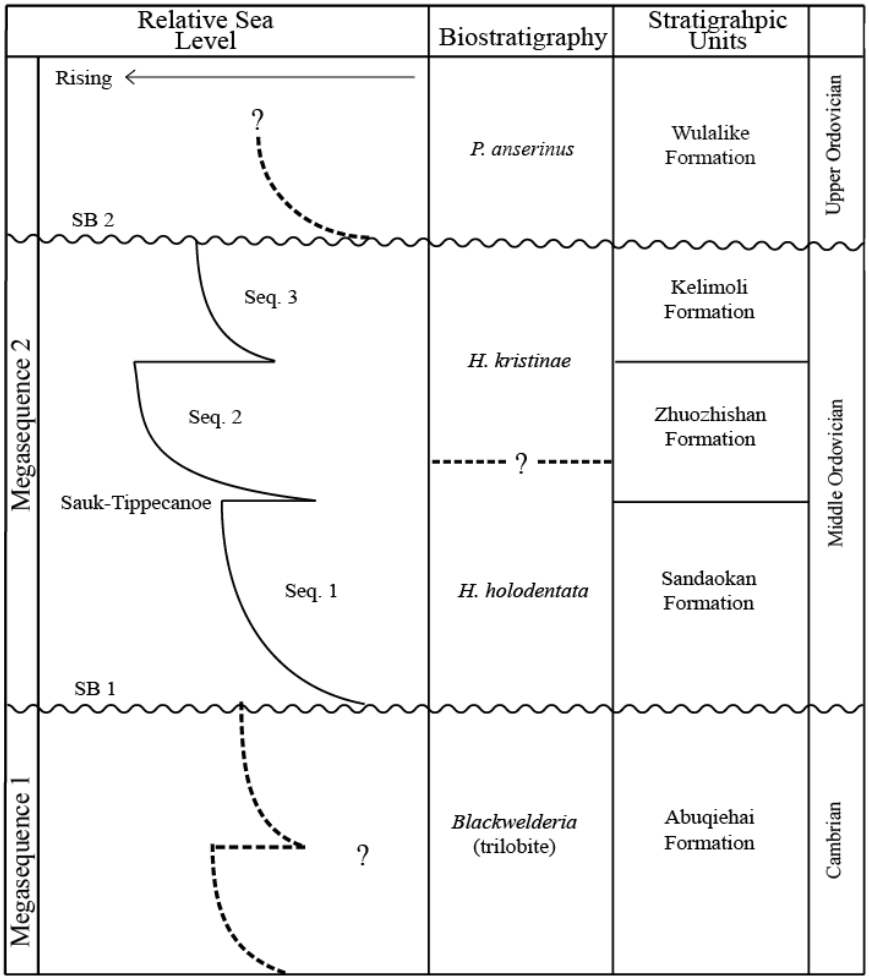

Figure 20. Sequence stratigraphy hypothesis 1, in which megasequence 2 is represented in its entirety in the NCB by three sequences. The Sandaokan Formation corresponds with sequence 1, the Zhuozhishan Formation corresponds with sequence 2, and the Kelimoli Formation corresponds with sequence 3. Note that the base of the Zhuozhishan Formation (top of sequence 1) corresponds with the North American Sauk-Tippecanoe megasequence boundary. SB1 lies at the base of the Sandaokan Formation, and SB2 lies above the Kelimoli Formation. Note that sequence stratigraphic lines are dotted in Cambrian and the Upper Ordovician because the relationship between lithology and sequence stratigraphy is unknown in the NCB for these intervals. Additionally, the precise location of the boundary between *H. holodentata* and *H. kristinae* is unknown but lies within the Zhuozhishan Formation.

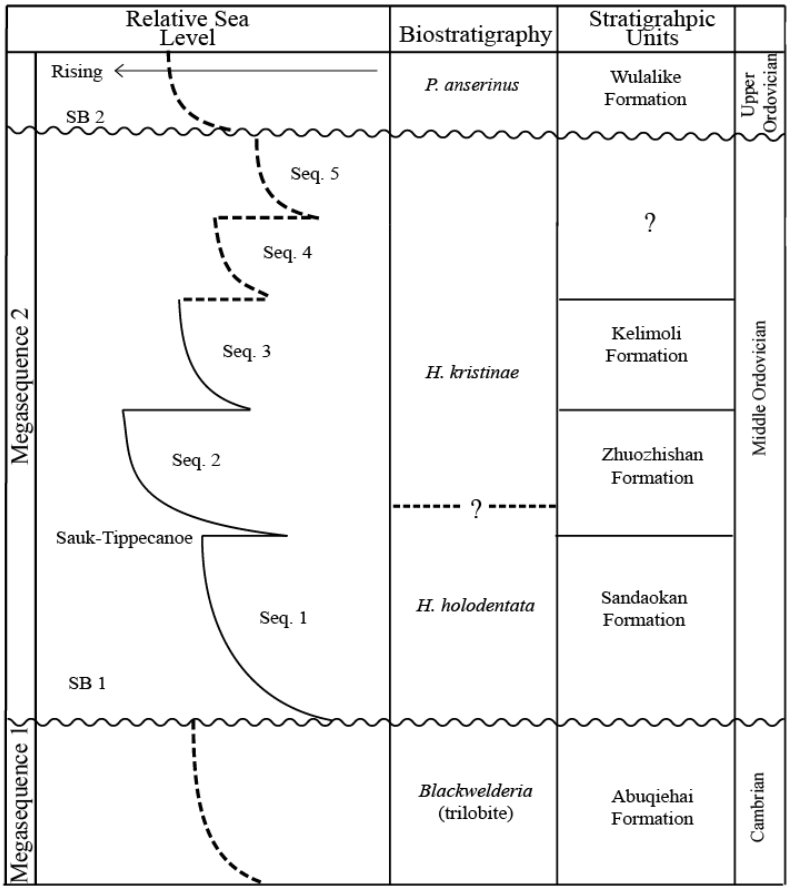

Figure 21. Sequence stratigraphy hypothesis 2, in which megasequence 2 is comprised of more than three sequences. Sequences 4 and 5 are added hypothetically by dotted lines in order to illustrate that megasequence 2 could be incomplete in the NCB. These sequences may have been eroded, or they may have coincided with periods of nondeposition.

CONCLUSION

This study presents an integrated sedimentologic, biostratigraphic, and chemostratigraphic analysis of two localities of Middle Ordovician Kelimoli Formation in Inner Mongolia, China. Results indicate that strata at both localities were deposited in the Helan Aulacogen during the Dw2 or Dw3 stage slices of the Middle Ordovician on a carbonate apron, and are capped by distinctive breccia beds that correspond with global sea level fall, possibly associated with global cooling at the Middle-Upper Ordovician boundary (Ainsaar et al., 2010). These strata exhibit the Middle-Darriwilian Carbon Isotope Excursion (MDICE), which is recognized for the first time in Inner Mongolia. YXT contains peak MDICE values and the initial negative drift of the descending limb, while XLF only captures peak $\delta^{13}C$ values because the upper limb of the excursion seen at YXT was likely eroded by slumping or removed by erosion below the breccia unit. The disparity in thickness of the Kelimoli Formation at YXT and XLF can likely be explained by their position on the carbonate apron. Specifically, XLF contains a thicker sequence of interbedded mudstone and marl in addition to slumped beds and YXT contains no slumped beds and a thicker succession of black shale because YXT is located more proximal to the carbonate source, representing a thicker cross-section of the carbonate apron, while YXT is located proximal to the basin floor in deeper water on a relatively flat substrate.

Biostratigraphic and chemostratigraphic contributions of this study, combined with sequence stratigraphy work for the NCP and biostratigraphy from Inner Mongolia, allow for the proposal of a Middle–Upper Ordovician sequence stratigraphic framework for Inner Mongolia (Meng et al., 1997; Wang et al., 2013). Specifically, the disconformity

between the base of the Sandaokan Formation and Cambrian Abuqiehai Formation contains SB1. The Sandaokan, Zhouzhishan, and Kelimoli formations represent sequences one, two, and three of megasequence 2, respectively. The contact between the Zhouzhishan and Kelimoli formations temporally corresponds with the North American Sauk-Tippecanoe megasequence boundary, and the disconformity between the Kelimoli Formation and overlying Wulalike Formation likely corresponds with SB2 and the Middle-Upper Ordovician boundary. The Sandaokan Foramtion contains the rising limb of MDICE, and the Kelimoli Formation contains peak MDICE values and the beginning of the descending limb; a detailed chemostatigraphic analysis of the Zhuozhishan Formation would likely contain the missing part of MDICE in the NCB, and further biostratigraphic analysis of Zhuozhishan and the Kelimoli formations (pending results at the time of printing) will aid in testing this proposed sequence stratigraphic framework for the NCB.

REFERENCES

Ainsaar, L., Meidla, T., Tinn, O., Martma, T., Dronov, A., 2007, Iiwilian (Middle Ordovician) carbon isotope stratigraphy in Baltoscandia: Acta Palaeontologica Sinica, Supplement 46, p. 1-8.

Ainsaar, L., Meidla, T., Tinn, O., 2004, Middle and Upper Ordovician stable isotope stratigraphy across the facies belts in the East Baltic, in Hints, O., and Ainsaar, L., eds., Conference Materials: Tartu University Press, Tartu, p. 11-12.

Ainsaar, L., Kaljo, D., Martma, T., Meidla, T., Mannik, P., Nolvak, J., Tinn, O., 2010, Middle and Upper Orovician carbon isotope chemostratigraphy in Baltoscandia: a correlation tool and clues to environmental history: Palaeogeography, Palaeoclimatology, Palaeoecology, v. 294, p. 189-201.

Albanesi, G. L., Bergstrom, S. M., Schmitz, B., Serra, F., Feltes, N. A., Voldman, G. G., Ortega, G., 2013, Darriwilian (Middle Ordovician) $\delta^{13}C$ chemostratigraphy in the Precordillera of Argentina: Documentation of the middle Darriwilian Isotope Carbon Excursion (MDICE) and its use for intercontinental correlation: Paleogeography, Palaeoclimatology, Palaeoecology, v. 389, p. 48-63.

Bauer, J. A., 1989, Conodont Biostratigraphy and Paleoecology of Middle Ordovician Rocks in Eastern Oklahoma: Journal of Paleontology, v. 63, p. 92-107.

Bergstrom, S. M., Chen, X., Guiterrez-Marco, J. C., Dronov, A., 2009, The new chronostratigraphic classification of the Ordovician System and its relations to major regional series and stages and to $\delta^{13}C$ chemostratigraphy: Lethaia, v. 42, p. 97-107.

Bian, Q., Gao, S., Li, D., Ye, Z., Chang, C., Luo, X., 2001, A Study of the Kunlun-Qilian-Qinling Suture System: Acta Geologica Sinica-English Edition, v. 75, p. 364-374.

Buggisch, W., Keller, M., Lehnert, O., 2003, Carbon isotope record of Late Cambrian to early Ordovician carbonates of the Argentine Precordillera: Palaeogeography, Palaeoclimatology, Palaeoecology, v. 195, p. 357-373.

Calner, M., Lehnert, O., Wu, R., Dahlqvist, P., Joachimski, M., 2014, d13C chemostratigraphy in the Middle-Lower Ordovician succession of Oland (Sweden) and the global significance of MDICE: GFF{???????], v. 136, p. 48-54.

Chough, S.K., Lee, H.S., Woo, J., Chen, J., Choi, D.K., Lee, S.-b., Kang, I., Park, T.-y., Han, Z., 2010, Cambrian stratigraphy of the North China Platform: revisiting principal sections in Shandong Province, China: Geosciences Journal, v. 14, p. 235-268.

Darby, B., & Ritts, B., 2002, Mesozoic contractional deformation in te middle of the Asian tectonic collage: the intraplate Western Ordos fold—thrust belt, China: Earth and Planetary Science Letters, v. 205, p. 13-24.

Drzewiecki, P. A., Simo, J. A., 2002, Depositional processes, triggering mechanisms and sediment composition of carbonate gravity flow deposits: examples from the Late Cretaceous of the south-central Pyrenees, Spain: Sedimentary Geology, v. 146, p. 155-189.

Edwards, C. T., Saltzman, M. R., 2014, Carbon isotope ($\delta^{13}C$) stratigraphy of the Lower-Middle Ordovician (Tremadocian-Darriwilian) in the Great Basin, western United States: Implications for global correlation: Palaeogeography, Palaeoclimatology, Palaeoecology, v. 399, p. 1-20.

Ethington, R. L., 2012, Conodont Biostratigraphy Across a Conformable Sauk-Tippecanoe Megasequence Boundary, Western Central Utah: Geologic Society of America Abstract, v. 44, no. 5, p. 1.

Finney, S., Ethington, R., Repetski, J., 2007, The boundary between the Sauk and Tippecanoe Sloss sequences of North America: Acta Palaeontologica Sinica, Supplement, v. 46, p. 128-134.

Huang, B., Zhu, R., Otofuji, Y., and Yang, Z., 2000, The early Paleozoic paleogeography of the north China Block and the other major blocks of China: Chinese Science Bulletin, v. 45, p. 1057–1065.

Kaljo, D., Martma, T., Saadre, T., 2007, Post-Hunnebergian Ordovician carbon isotope trend in Baltoscandia, its environmental implications and some similarities with that of Nevada: Palaeogeography, Palaeoclimatology, Palaeoecology, v. 245, p. 138-155.

Lee, H.S., and Chough, S.K., 2011, Depositional processes of the Zhushadong and Mantou formations (Early to Middle Cambrian), Shandong Province, China: roles of archipelago and mixed carbonate–siliciclastic sedimentation on cycle genesis during initial flooding of the North China Platform: Sedimentology, v. 58, p. 1530-1572.

Leslie, S., Saltzman, M., Bergstrom, S., Repetski, J., Howard, A., Seward, A., 2011, Conodont Biostratigraphy and Stable Isotope Stratigraphy across the Ordovician Knox/Beekmantown Unconformity in the Central Appalachians: in *Ordovician of the World*, p. 301-308.

Lin, C., Yang, Q., Li, S., Li, Z., 1991, Sedimentary characteristics of the Early Paleozoic deep water gravity fow systems and basin filling style in the Helan Aulacogen, Northwest China: Geoscience, v. 5, p. 252-263. (In Chinese with English abstract)

Liu, B., Wang, Y., Qian, X., 1997, Two Ordovician Unconformities in North China: Their Origins and Relationships to Regional Carbonate-Reservior Characteristics: Carbonates and Evaporites, v. 12, p. 177-184.

Lowe, D. R., 1982, Sediment gravity flows: II. Depositional models with special reference to the deposits of high-density turbidity currents: Journal of Sedimentary Petrology, v. 46, p. 188-199.

Martma, T., 2005, Ordovician carbon isotopes: Estonian Geological Survey Bulletin, v. 6, p. 25-27.

McKenzie, R.N., Hughes, N.C., Myrow, P.M., Choi, D.K, 2011. Trilobites and zircons link north China with the eastern Himalaya during the Cambrian: Geology, v. 39, p. 591–594; doi:10.1130/G31838.1.

Meidla, T., Ainsaar, L., Backman, J., Dronov, A., Holmer, L., Sturesson, U., 2004, Middle-Upper Ordovician carbon isotope record from Vastergotland (Sweden) and East Baltic, in Hints, O., and Ainsaar, L., eds., Conference Materials: Tartu University Press, Tartu, p. 67-68.

Meng, X., Ge, M., Tucker, M.E., 1997, Sequence stratigraphy, sea-level changes and depositional systems in the Cambro-Ordovician of the North China carbonate platform: Sedimentary Geology, v. 114, p. 189–222.

Munnecke, A., Zhang, Y., Liu, X., Cheng, J., 2001, Stable carbon isotope stratigraphy in the Ordovician of South China: Palaeogeogrpahy, Palaeoclimatology, Palaeoecology, v. 307, p. 17-43.

Mullins, H., Cook, H., 1986, Carbonate Apron Models: Alternatives to the Submarine Fan Model for Paleoenvironmental Analysis and Hyrocarbon Exploration: Sedimentary Geology, v. 48, p. 37-79.

Myrow, P. M., Chen, J., Snyder, Z., Leslie, S., Fike, D. A., Fanning, C. M., Yuan, J., Tang, P., *in press*, Depositional history, tectonics, and provenance of the Cambrian-Ordovician boundary interval in the western margin of the North China block: Palaeogeography, Palaeoclimatology, Palaeoecology.

Myrow, P. M., 1990, A new graph for understanding colors of mudrocks and shales: Journal of Geological Education, v. 38, p. 16-20.

Pomar, L., Brandano, M., 2004, Environmental factors influencing skeletal grain sediment associations: a critical review of Miocene examples from the western Mediterranean: Sedimentology, v. 51, p. 627-651.

Ripperdan, R., 2001, Stratigraphic Variation in Marine Carbonate Carbon Isotope Ratios: Mineralogy and Geochemistry, v. 43, no. 1, p. 637-662.

Schmitz, B., Bergstrom, S. M., Xiogeng, W., 2010, The middle Darriwilian (Ordovician) $\delta^{13}C$ excursion (MDICE) discovered in the Yangtze Platform succession in China: implications of its first recorded occurrences outside Baltoscandia: Journal of the Geological Society, London, v. 167, p. 249-259.

Sial, A., Peralta, S., Gaucher, C., Toselli, A., Ferreira, V., Frei, R., Parada, M., Pimentel, M., Pereira, N., 2013, High-resolution stable isotope stratigraphy of the upper Cambrian and Ordovician in the Argentine Precordillera: carbon isotope excursions and correlations: Gondwana Research, v. 24, p. 330-348.

Snyder, Z., 2013, Cambrian–Ordovician stratigraphy and paleogeography of the western margin of the North China Block: Senior Thesis, Colorado College, p. 1-106.

Spaletti, L. A., Cingolani, C. A., Varela, R., Cuerda, A. J., 1989, Sediment gravity flow deposits of an Ordovician deep-sea fan system (western Precordillera, Argentina): Sedimentary Geology, v. 61, p. 287-301.

Stow, A. V., 1986, Deep clastic seas: In: Sedimentary Environments and Facies (Ed. By H. G. Reading) pp.399-444. Blackwells, Oxford.

Stow, A. V., Mayall, M., 2000, Deep-water sedimentary systems: New models for the 21st century: Marine and Petroleum Geology, v. 17, p. 125-135.

Stouge, S., 1984, Conodonts of the Middle Ordovician Table Head Formation, western Newfoundland: Fossils and Strata, no. 16, 145 p.

Sun, G., Liu, J., 1983, Helan Aulacogen and front basin and their evolution: Oil and gas Geology, v. 4, p. 236-245. (In Chinese with English abstract)

Thompson, C., Kah, L. C., 2012, Sulfur isotope evidence for widespread euxinia and fluctuating oxycline in Early to Middle Ordovoician greenhouse oceans: Palaeogeography, Paleoclimatology, Paleoecology, v. 313-314, p. 189-214.

Tucker, M. E., Wright, P. V., 1990, Carbonate Sedimentology: Blackwell Scientific Publications, XX p.

Wang, Z., Stig, M., Zhen, Y., Chen, X., Zhang, Y. D., 2013, On the integration of Ordovician conodont and graptolite biostratigraphy: New examples from Gansu and Inner Mongolia in China: Alcheringa, v. 37, p. 510-528.

Zhang, T., Shen, Y., Algeo, T., 2010, High-resolution carbon isotope records from the Ordovician of South China: links to climatic cooling and the Great Ordovician Biodiversification event (GOBE): Palaeogeography, Palaeoclimatology, Palaeoecology, v. 289, p. 102-112.

APPENDICES TO THE TEXT

Appendix A. Detailed Stratigraphic Column for YXT

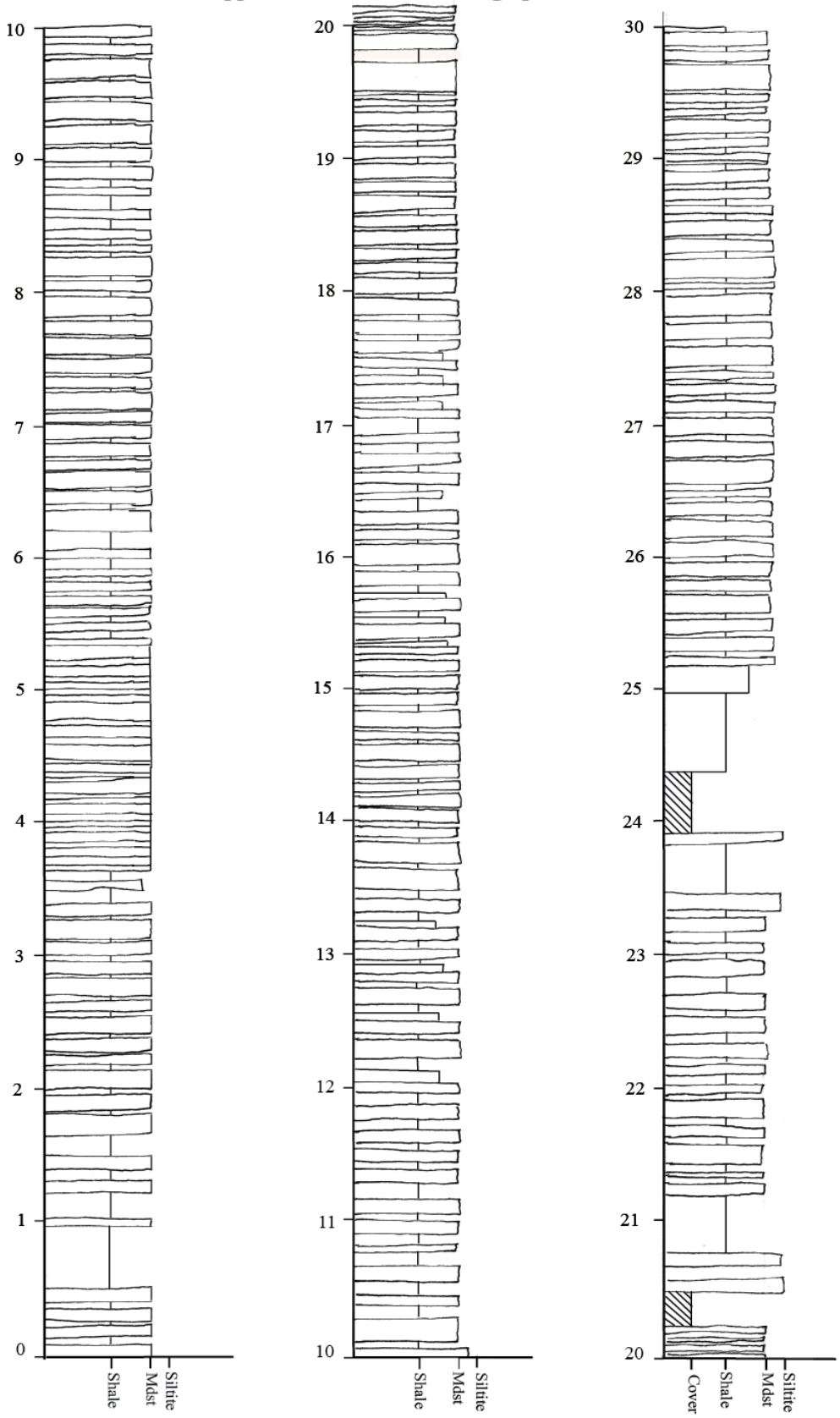

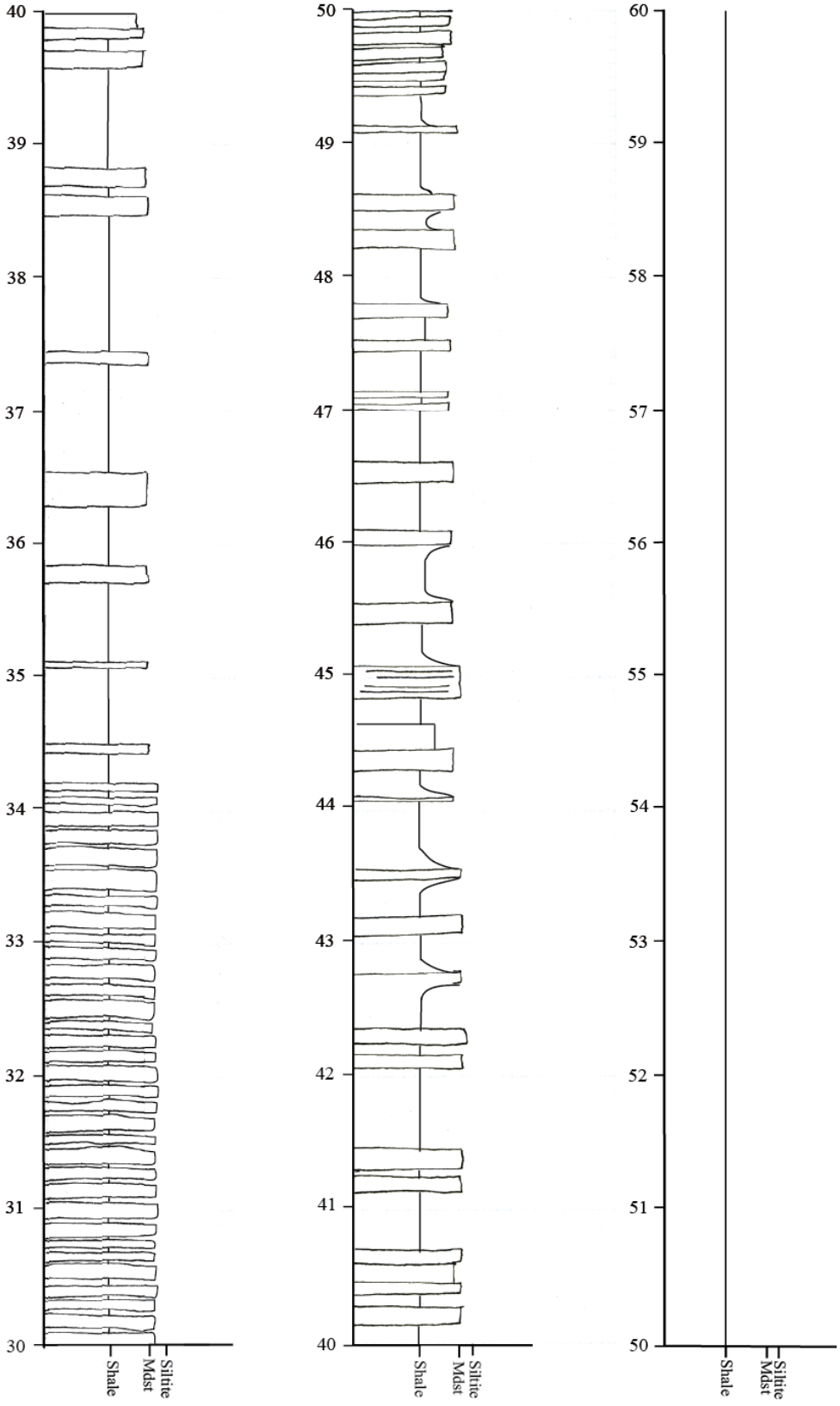
40
39
38
37
36
35
34
33
32
31
30
Shale
Mdst
Siltite
50
49
48
47
46
45
44
43
42
41
40
Shale
Mdst
Siltite
60
59
58
57
56
55
54
53
52
51
50
Shale
Mdst
Siltite

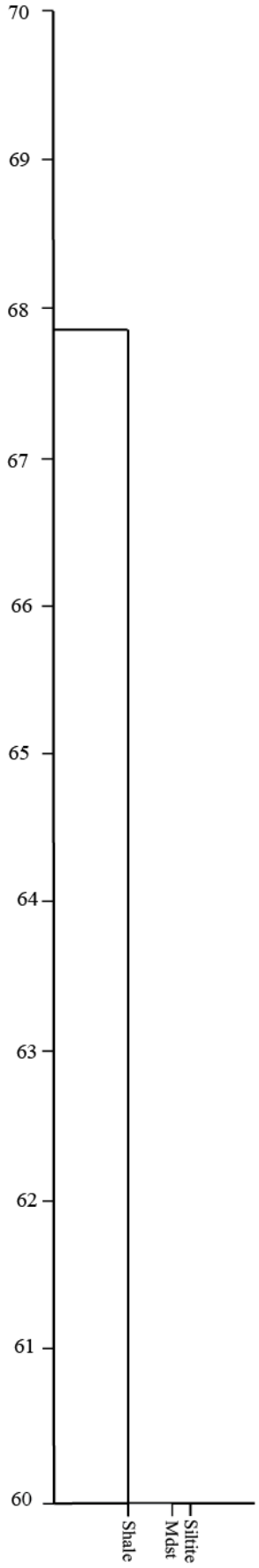
70
69
68
67
66
65
64
63
62
61
60
Shale
Mdst
Siltite

Appendix B. XLF Detailed Stratigraphic Column

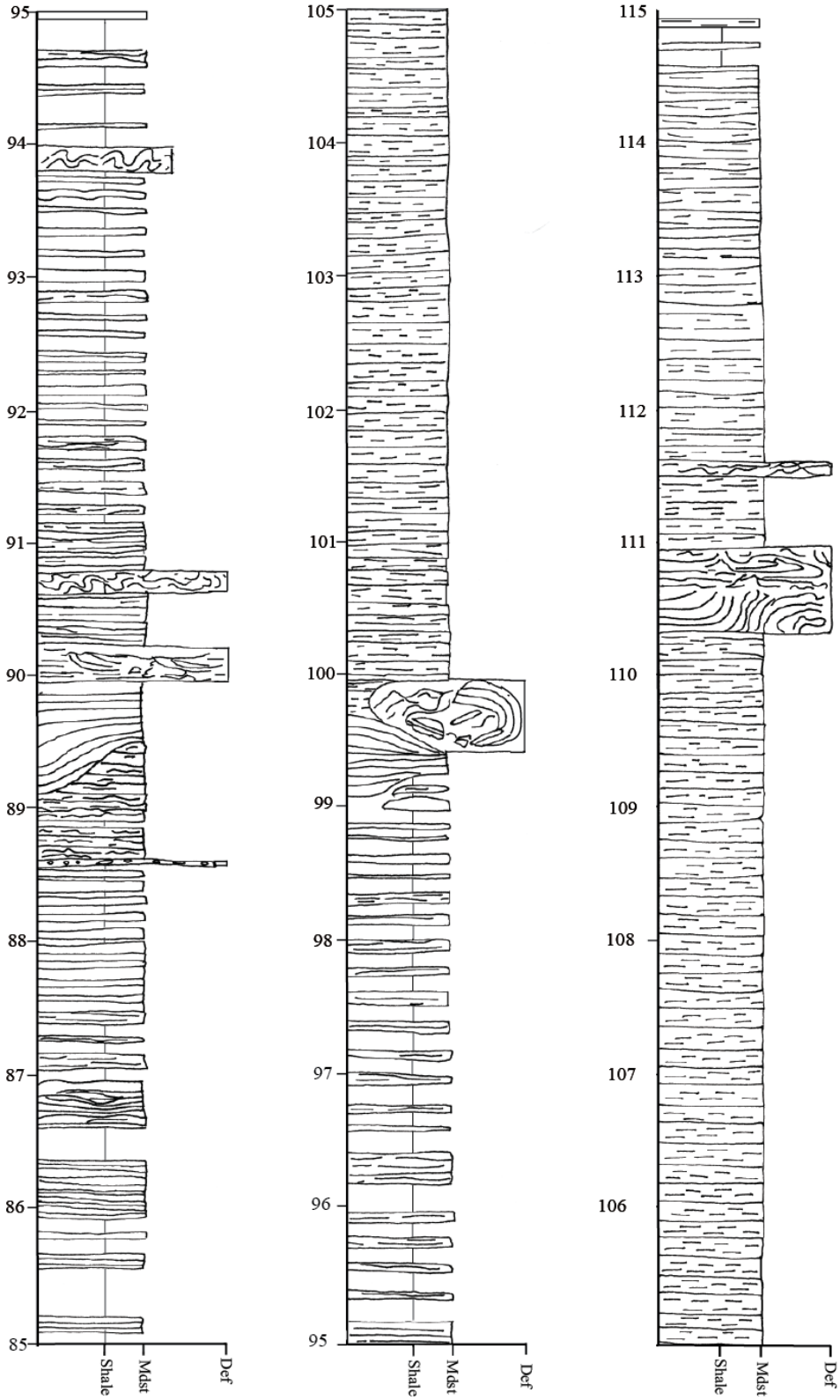

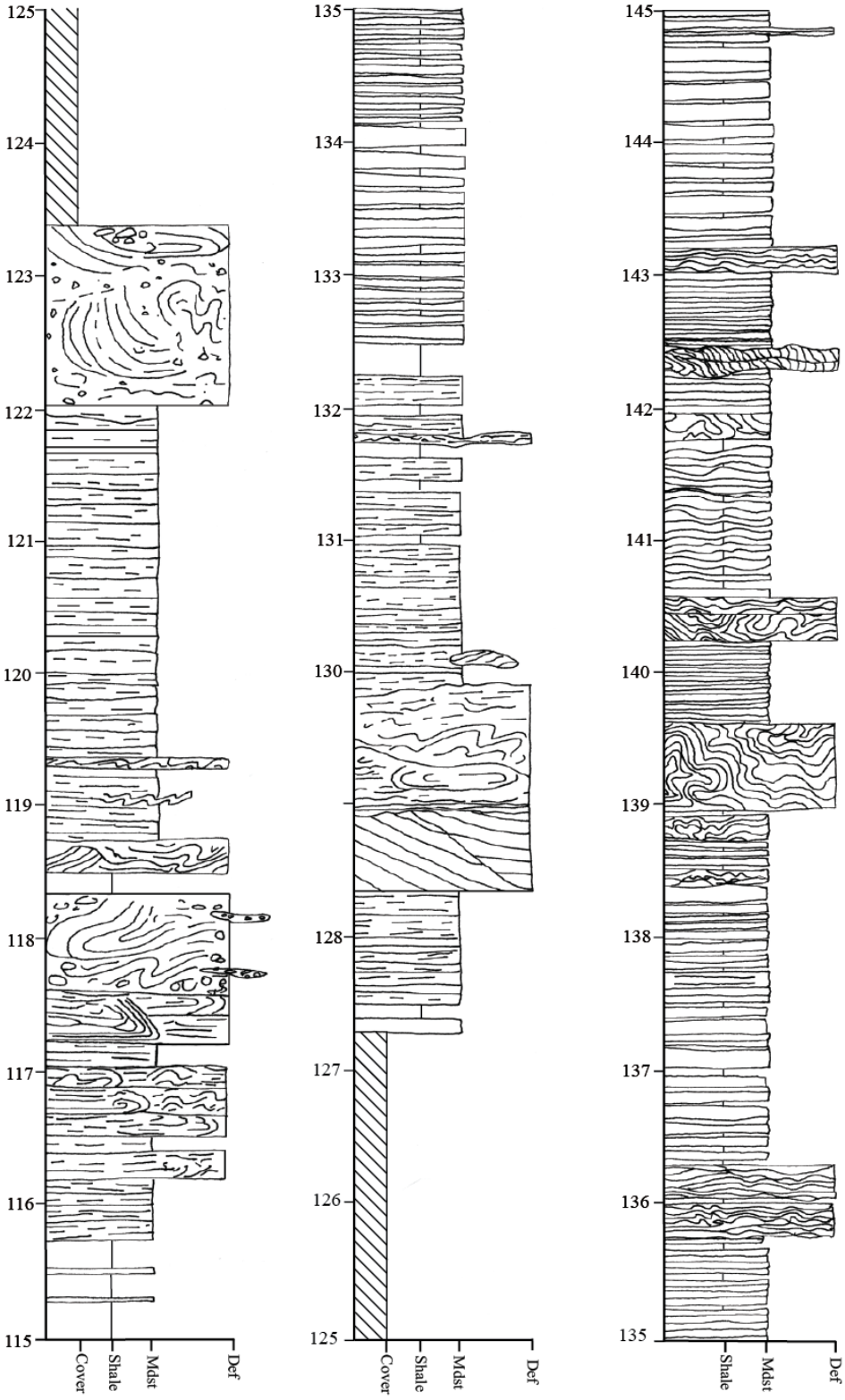
125
124
123
122
121
120
119
118
117
116
115
Cover
Shale
Mdst
Def
135
134
133
132
131
130
128
127
126
125
Cover
Shale
Mdst
Def
145
144
143
142
141
140
139
138
137
136
135
Shale
Mdst
Def

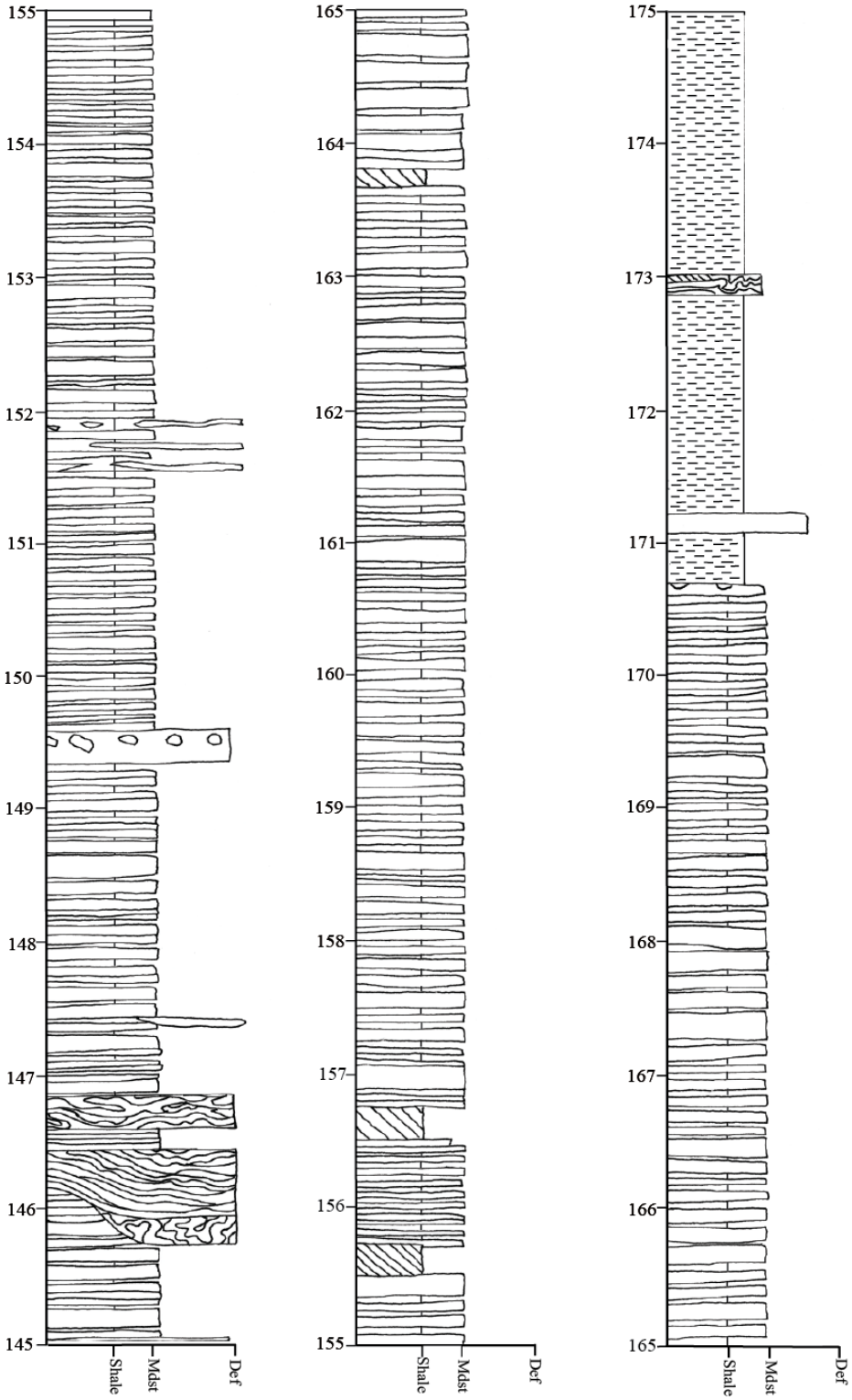
155
154
153
152
151
150
149
148
147
146
145
Shale
Mdst
Def
165
164
163
162
161
160
159
158
157
156
155
Shale
Mdst
Def
175
174
173
172
171
170
169
168
167
166
165
Shale
Mdst
Def

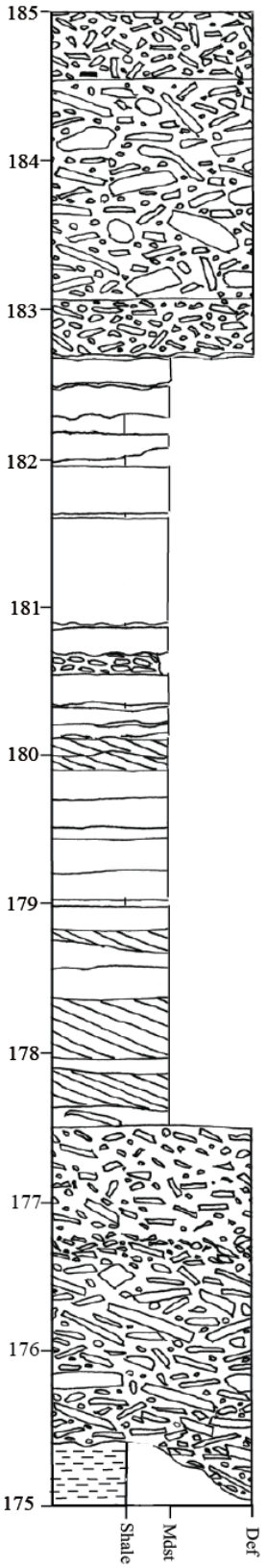
185
184
183
182
181
180
179
178
177
176
175
Shale
Mdst
Def